

Kerr black holes with synchronised Proca hair: lensing, shadows and EHT constraints

Ivo Sengo^{*1}, Pedro V.P. Cunha^{†1}, Carlos A. R. Herdeiro^{‡1}, and Eugen Radu^{§1}

¹Departamento de Matemática da Universidade de Aveiro and Centre for Research and Development in Mathematics and Applications (CIDMA), Campus de Santiago, 3810-183 Aveiro, Portugal

September 2022

Abstract

We investigate the gravitational lensing by spinning Proca stars and the shadows and lensing by Kerr black holes (BHs) with synchronised Proca hair, discussing both theoretical aspects and observational constraints from the Event Horizon Telescope (EHT) M87* and Sgr A* data. On the theoretical side, this family of BHs interpolates between Kerr-like solutions – exhibiting a similar optical appearance to that of Kerr BHs – to very non-Kerr like solutions, exhibiting exotic features such as cuspy shadows, egg-like shadows and ghost shadows. We interpret these features in terms of the structure of the fundamental photon orbits, for which different branches exist, containing both stable and unstable orbits, with some of the latter not being shadow related. On the observational side, we show that current EHT constraints are compatible with all such BHs that could form from the growth of the superradiant instability of Kerr BHs. Unexpectedly, given the (roughly) 10% error bars in the EHT data – and in contrast to their scalar cousin model –, some of the BHs with up to 40% of their energy in their Proca hair are compatible with the current data. We estimate the necessary resolution of future observations to better constrain this model.

*sengo@ua.pt

†pvcunha@ua.pt

‡herdeiro@ua.pt

§eugen.radu@ua.pt

Contents

1	Introduction	2
2	The solutions	4
3	Setup	5
4	Lensing by Proca Stars	6
5	Lensing by KBHsPH	9
6	Fundamental photon orbits	12
6.1	Overview	12
6.2	Analyzing lensing images using FPOs	13
7	Analyzing the astrophysically viable space of solutions	17
8	Constraining the hair using M87* data	19
8.1	Approximation formula for the shadow viewed from 17° inclination	19
8.2	Application to the M87* BH shadow	21
9	Constraining the hair using Sgr A* data	24
10	Conclusions and Discussion	25
A	Physical quantities of selected solutions	35

1 Introduction

The present golden age of observational strong gravity invites us to test the Kerr hypothesis and, in particular, its universality [1]. It is therefore timely to consider well motivated non-Kerr models and compare their phenomenology with the current data. In parallel, considering non-Kerr models is a valuable theoretical arena, often enlightening in understanding how generic or special the General Relativity (GR) (electro-)vacuum black holes (BHs) are, since much of our intuition about the physics of BHs is constructed upon them.

For either of these – *i.e.* observational or theoretical – perspectives, light is a privileged probe. It has been so since the genesis of GR, when the bending of light was proposed as a test [2], and its confirmation [3] elevated GR above Newton’s law. Einstein himself studied gravitational lensing and the possibility of multiple images, including what we now call *Einstein rings* [4]. The deeper understanding of BHs that emerged in the 1960s, in particular the discovery of the Kerr metric [5], led to the first (academic) discussions on the optical appearance of BHs [6]. It was understood that such optical appearance is intimately connected to the bound orbits of light around BHs. When planar, these orbits are called *light rings*, which have been well understood for the Kerr BH since the 1970s [7]. The non-planar bound orbits of light around Kerr BHs are called *spherical photon orbits* (SPOs) and have been studied in detailed only more recently [8]. For generic non-Kerr spacetimes, in particular

where the geodesic motion may not be integrable, we shall call such bound orbits of light *fundamental photon orbits* (FPOs), following [9].

These academic studies were accompanied by more astrophysical investigations on the optical appearance of BHs, most notably the *tour de force* image of a Schwarzschild BH surrounded by an accretion disk, by Luminet [10]. At the turn of the last century Falcke *et al.* proposed that the optical appearance the supermassive BH at our galactic centre could actually be resolved, to produce its “photography”, observing in particular its silhouette or *shadow* [11]. This remarkable proposal led to a worldwide collaborative effort – the *Event Horizon Telescope* (EHT) – that in 2019 [12–14] and 2022 [15–18] published the first images of the M87* and Sgr A* supermassive BHs, respectively.

BH imaging is still in its infancy, and the future promises to deliver higher accurate results with the next generation EHT observatories. It is therefore timely to study how much these observations can distinguish well motivated models of non-Kerr BHs, emerging as solutions of sound physical theories, without known pathologies and with a plausible formation mechanism. Such conditions are quite restrictive, but they can be met even in GR with simple matter contents obeying the most fundamental energy conditions. This is the case of Kerr BHs with (synchronised) Proca Hair (KBHsPH) [19, 20] that are solution of Einstein’s gravity minimally coupled to a free, complex Proca field (*cf.* action 1 below). These BHs circumvent no-Proca hair theorems [21] by virtue of a harmonic time dependence of the bosonic field [19]. The model is free of known pathologies, and the hairy BHs could emerge dynamically via the superradiant instability of Kerr [22], triggered by the bosonic field [23–25]. This family of hairy BHs interpolates between the bald Kerr solution and horizonless self-gravitating solitons known as *Proca stars* (PSs) [26]. Spinning PSs, unlike their scalar cousins - boson stars (BSs) - have been shown to be dynamically robust [27], lending further dynamical credibility to the model - see also [28]. These PSs, moreover, have been recently advocated to match gravitational wave data [29, 30], further motivating the model from a phenomenological viewpoint. Finally, even in the spherical case, PSs exhibit qualitatively distinct features from their scalar cousins, and have been shown to be able to imitate imaging observations under some conditions [31] (see also [32]).

The goal of this paper is study the lensing, shadows of KBHsPH from both a theoretical and observational viewpoint. This study parallels previous studies for Kerr BHs with (synchronised) scalar hair [9, 33–36], and some of our findings are qualitatively similar to the scalar case; others, however, are different. We observe, for instance, that the shadows of these Proca hairy BHs can vary from Kerr-like to very non-Kerr like, as one scans the domain of existence of solutions. When the latter occur, qualitatively distinct features emerge, such as cuspy shadows, egg-like shadows and ghost shadows. We shall interpret these features considering the study of the FPOs of the corresponding solutions. One of the most unexpected aspects of our study emerges when considering the comparison with EHT data. As we shall show below, KBHsPH can be compatible with the current EHT observations for much hairier solutions than in the scalar case. We shall put forward a speculation to why this is the case in the discussion section.

This paper is organized as follows. Sections 2 and 3 discuss generalities about the solutions and the setup for studying lensing and shadows. Then, sections 4–6 discuss theoretical aspects, namely the lensing by PSs, the shadows and lensing obtained by KBHsPH from ray-tracing and the FPOs structure for some chosen solutions. In sections 7–9 we turn to observational aspects, developing a

setup for comparing solutions in a region of interest of the domain of solutions and using the EHT M87* and Sgr A* data to constrain the parameter space. Finally, in section 10 we offer some conclusions and a discussion.

2 The solutions

KBHsPH [19, 20] are fully non-linear solutions of the Einstein-complex-Proca model, described by the action

$$S = \int d^4x \sqrt{-g} \left(\frac{R}{16\pi} + \mathcal{L}_M \right), \quad (1)$$

where g is the determinant of the metric, R is the Ricci scalar and \mathcal{L}_M is the Lagrangian density of a massive complex vector boson A^α , which reads:

$$\mathcal{L}_M = -\frac{1}{4} F_{\alpha\beta} \bar{F}^{\alpha\beta} - \frac{1}{2} \mu^2 A_\alpha \bar{A}^\alpha. \quad (2)$$

In Eq. (2), $F_{\alpha\beta} = 2A_{[\beta;\alpha]}$ is the electromagnetic-field tensor, which is antisymmetric and gauge invariant, $\alpha, \beta = \{0, 1, 2, 3\}$, μ is the boson's mass and overbar denotes complex conjugation.

Varying the action (1) one obtains the Einstein field equations sourced by the Proca energy-momentum tensor, as well as the Proca equations for the boson field – see [19, 20] for a detailed discussion of the Einstein-complex-Proca model. This system of equations can be solved numerically by considering the following metric ansatz for stationary and axially-symmetric BH solutions (as well as for horizonless, self-gravitating solitons):

$$ds^2 = -e^{2F_0} N dt^2 + e^{2F_1} \left(\frac{dr^2}{N} + r^2 d\theta^2 \right) + e^{2F_2} r^2 \sin^2 \theta (d\phi - W dt)^2, \quad (3)$$

where $N = 1 - r_H/r$ and F_i, W ($i = 0, 1, 2$) are functions of the spheroidal coordinates (r, θ) . The parameter r_H is the radial coordinate of the event horizon; when it is set to zero, the solutions describe spinning PSs. The metric possesses two Killing vector fields $\partial/\partial t$ and $\partial/\partial \phi$, connected respectively to stationarity and axial-symmetry. In addition, a \mathbb{Z}_2 reflection symmetry around the equatorial plane ($\theta = \pi/2$) will be assumed. For the Proca potential it is considered an ansatz of the form

$$A = e^{i(m\phi - \omega t)} (iV dt + H_1 dr + H_2 d\theta + iH_3 \sin \theta d\phi), \quad (4)$$

where the four functions (V, H_i) all depend on (r, θ) . This ansatz has an harmonic time and azimuthal dependence, associated with the frequency $\omega > 0$ and the azimuthal harmonic index $m \in \mathbb{Z}$, respectively.

We are going to focus on fundamental ¹ KBHsPH solutions, which were first discussed in [24] and reported in detail in [20]. The domain of existence of these solutions is displayed in Fig. 1, where hairy

¹These are solutions with a nodeless Proca potential temporal component V , and $m = 1$. These solutions are the ones that bifurcate from the linear bound state of a test Proca field around a Kerr BH, that corresponds to the lowest energy state.

BHs solutions exist on a bound set (blue shaded region), bounded above by the existence line of PS solutions (solid red line) and below by a set of Kerr BHs (blue dashed line).

The solutions featured in this paper are identified by a symbol of the form $u.v$, with $u, v \in \mathbb{N}_0$. Solutions with the same u share the same frequency (the greater the u , the smaller is the frequency), whilst the v index is related to the amount of hair within the solution (for the same u , hairier solutions have the smallest v). In this notation, PSs are identified by a symbol of the form $u.0$.

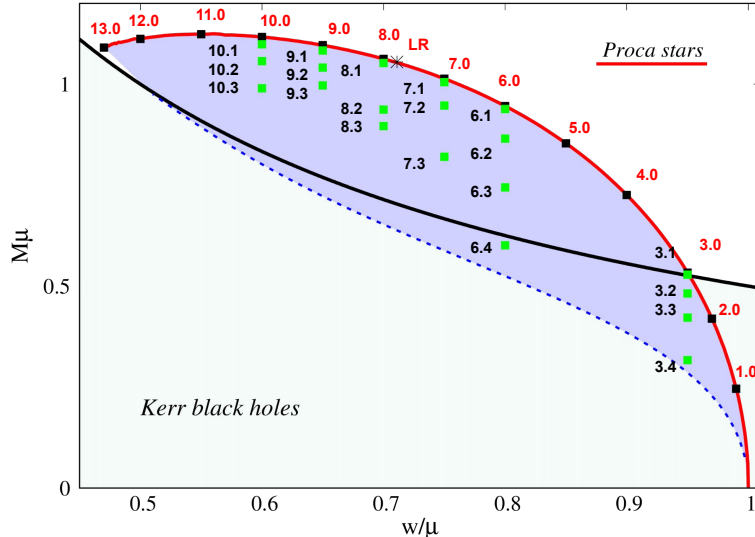


Figure 1: The domain of existence of KBHsPH (blue shaded region) and the corresponding PSs (red line). The asterisk symbol on the PS line marks the first PS solution to feature a light ring (LR) orbit. The relevant physical quantities of these solutions can be found in Appendix A

We remark that in order for the KBHsPH we have just described to be in the astrophysical BHs mass range, then the boson mass μ should be ultralight, *i.e.* $\mu \lesssim 10^{-10}$ eV. Such ultralight bosons are dark matter candidates under the fuzzy dark matter paradigm and could emerge in beyond the standard model scenarios – see the discussions in [37, 38].

3 Setup

The generation of synthetic lensing images of PSs and KBHsPH can be obtained by numerically evolving null-geodesics, which describes light motion in the high frequency limit. These synthetic images correspond to what an observer (\mathcal{O}), located at an off-centered position inside a celestial sphere, would see as a consequence of the gravitational lensing caused by the presence of a PS or BH placed at the center of that same sphere (Fig. 2, left panel).

Synthetic lensing images were generated by evolving numerically 1024×1024 light ray trajectories from \mathcal{O} 's location, using a *backwards ray-tracing* method [34, 39]. The observation angles seen by \mathcal{O} (in its frame) determine the initial conditions for the light ray propagation. The observer's field of view always spans 35° across both horizontal and vertical directions in all the lensing images presented in this paper. The image information is then presented in image coordinates (x, y) , obtained by multiplying the observation angles by the circumferential radius of the observer (defined below). This scaling procedure removes the typical fall-off behaviour of the angular size of objects at very large

distances - see [34] for more details.

To get a better grasp of the distortion introduced by either PSs or KBHsPH it is convenient to paint each of the quadrants of the celestial sphere by a different color, a setup introduced in [39] and popularized in [33].² Following [33], the point on the colored celestial sphere immediately in front of \mathcal{O} is marked by a white spot and dubbed \mathbf{F} . This white spot is apparent in the non-distorted field of view of such an observer, depicted in Fig. 2 (right panel) for reference.

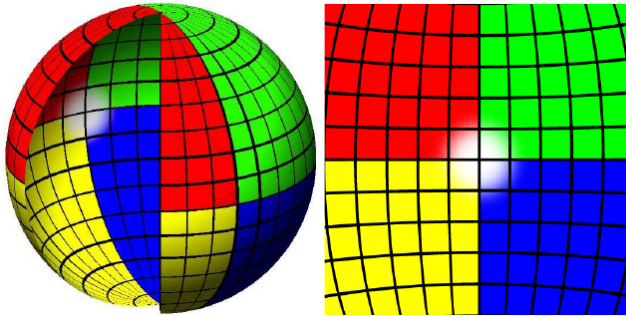


Figure 2: (Left) The full celestial sphere. (Right) Non-distorted field of view seen by the observer (flat spacetime). [Image adapted from [33]].

Unless otherwise stated, the lensing images that will be presented in the next sections are obtained assuming an observer on the equatorial plane ($\theta = \pi/2$) at a circumferential radius of $\tilde{r} = 15 M_{\text{ADM}}$, with the celestial sphere placed at twice this value. The *circumferential radius* \tilde{r} of some point \mathbf{A} (located on the equatorial plane) is a distance defined by:

$$\tilde{r} \equiv \frac{\mathcal{P}}{2\pi} = \sqrt{g_{\phi\phi}}. \quad (5)$$

\mathcal{P} is the circumference of the circle that includes point \mathbf{A} , with that circle determined by the orbits of the azimuthal Killing vector field ∂_ϕ on the equatorial plane. Hence, the value of \mathcal{P} can be obtained by the following integral:

$$\mathcal{P} = \int_0^{2\pi} \sqrt{g_{\phi\phi}} d\phi = 2\pi \sqrt{g_{\phi\phi}}. \quad (6)$$

Having concluded the discussion of the observation setup, we shall now move in the next section to PS lensing.

4 Lensing by Proca Stars

It is helpful to start with a discussion on the lensing due to PSs (see Fig. 3-5). To gain insight on the gravitational effects of the PSs, it is pedagogical to follow a sequence of solutions with increasingly stronger gravitational effects. Thus, we start from the PS solution 1.0, with $\omega^{1.0} = 0.99$, which is the closest one to vacuum (for which $\omega = 1$)³, and we then move along red spiral in the space of solutions, see Fig. 1.

For solution 1.0 we find no noticeable distortion on the background - Fig. 3 (top left panel) - when compared with the flat-spacetime reference image in Fig. 2. By moving to solutions 2.0 and 3.0 the

²This setup has been subsequently widely used *e.g.* [9, 32, 35, 40–54].

³For ease of notation we quote the frequencies of the solutions in units of μ ; *i.e.* $\omega/\mu \rightarrow \omega$.

(still very weak) lensing distortion only increases mildly - see Fig. 3 (top middle panel). Then, a new qualitative feature arises for solution 4.0 with $\omega_{ER1}^{4.0} = 0.90$: the appearance of the first Einstein ring, as the white spot at \mathbf{F} opens up and encloses two inverted copies of regions of the sky belonging to two of the quadrants of the celestial sphere - see Fig. 3 (top right panel).

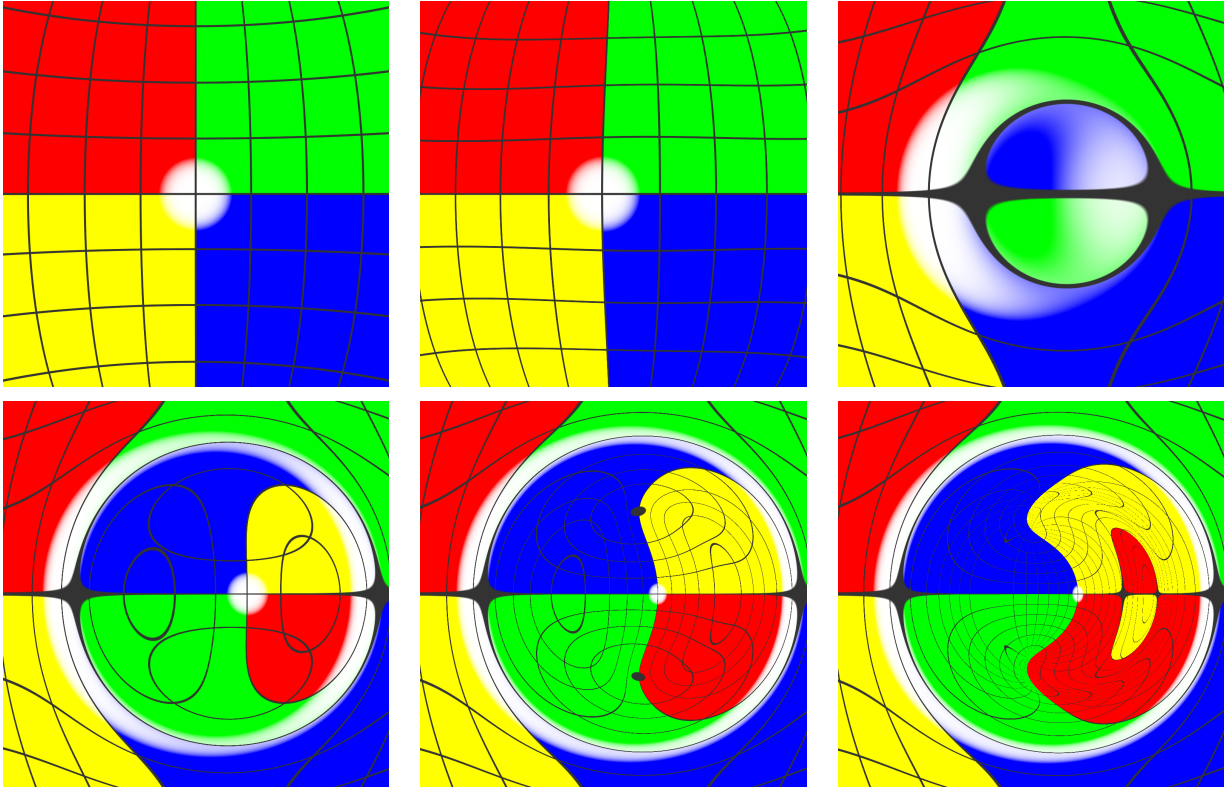


Figure 3: Lensing by PSs. From left to right: (top) $\omega^{1.0,3.0,4.0} = 0.99; 0.95; 0.9$; (bottom) $\omega^{5.0,6.0,7.0} = 0.85; 0.80; 0.75$.

As we move further along the spiral to solution 5.0, the Einstein ring takes a more elliptical shape and copies of all four quadrants can now be seen inside the ring - Fig. 3 (bottom left panel). Similarly to rotating scalar BSs [33], the side rotating away from \mathcal{O} appears more amplified, and \mathbf{F} is progressively shifted to one side. As we move even further along the PS spiral to solution 7.0 and $\omega_{ER2}^{7.0} = 0.75$, then we find the emergence of a second Einstein ring - see Fig. 3 (bottom right panel). Likewise to rotating BSs, these new rings also have a squashed "D-shape".

The first appearance of a light ring marks the transition from the compact to the ultra-compact regime [55]. This light ring appearance is observed (in our selection of solutions) for the PS solution 8.0, with $\omega_{LR1}^{8.0} = 0.70$, cf. Fig. 4 (top left panel); then an infinite number of copies - and a self similar structure - is expected to arise [39].

Even more compact PSs solutions start to exhibit image features that were shown to be associated with chaotic scattering in the scalar case [35]. Solutions 12.0 and 13.0, with respectively $\omega^{12.0} = 0.50$ and $\omega^{13.0} = 0.47$, are both examples of PSs that display these features - see Fig. 4 (bottom middle and right panels).

In addition, the authors in [35] discussed how (in the scalar case) there is a correlation between the chaotic pattern in the lensed image and a large integration time t , computed along null geodesics

of those regions. Following a similar analysis, we present in Fig. 5 the time-delay map associated to PS solutions 12.0 and 13.0 and, also here, a correlation between the integrated time and chaotic behaviour is apparent.

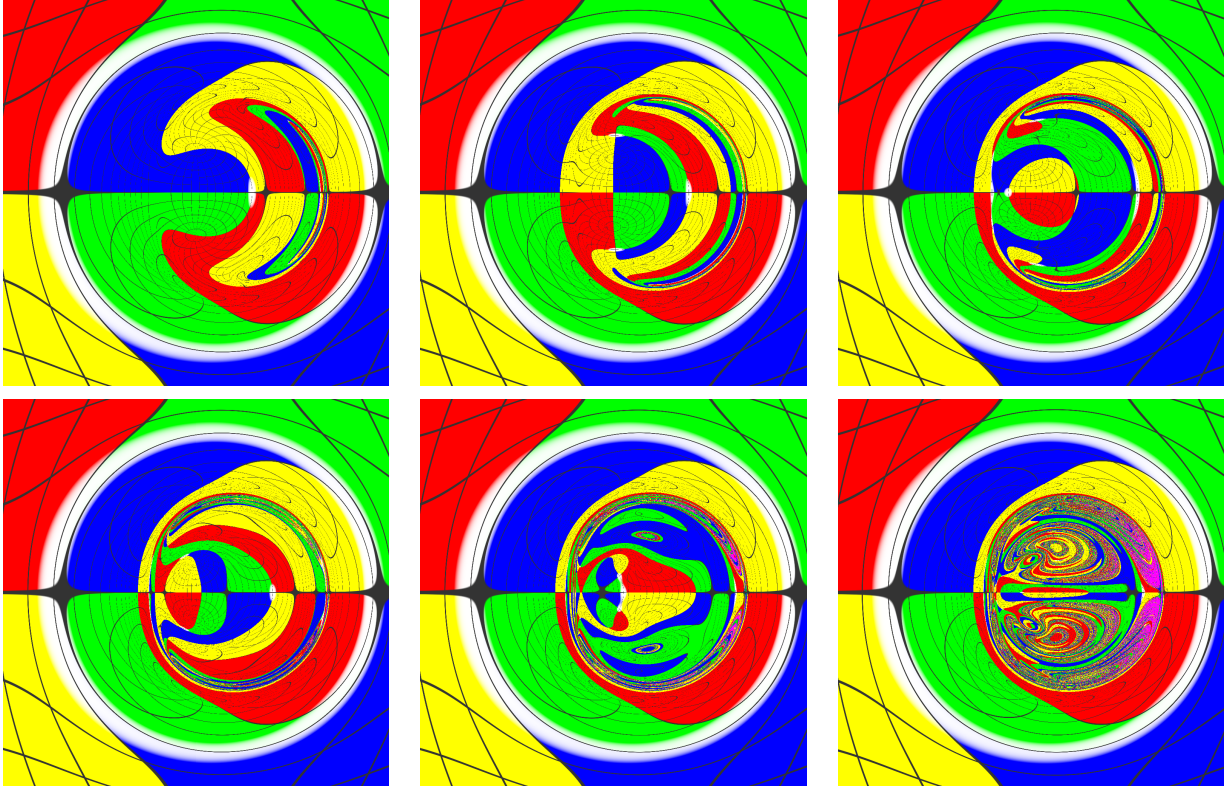


Figure 4: Lensing by ultra-compact PSs. From left to right: (top) $\omega^{8.0,9.0,10.0} = 0.70; 0.65; 0.60$; (bottom) $\omega^{11.0,12.0,13.0} = 0.55; 0.50; 0.47$. Note that the lensing images of solutions with $\omega^{12.0,13.0}$ show a few pink colored pixels. These pixels correspond to light rays whose integration time becomes so large that the endpoint cannot be resolved within the numerically allocated integration time, becoming trapped into *pockets* of the effective potential [35].

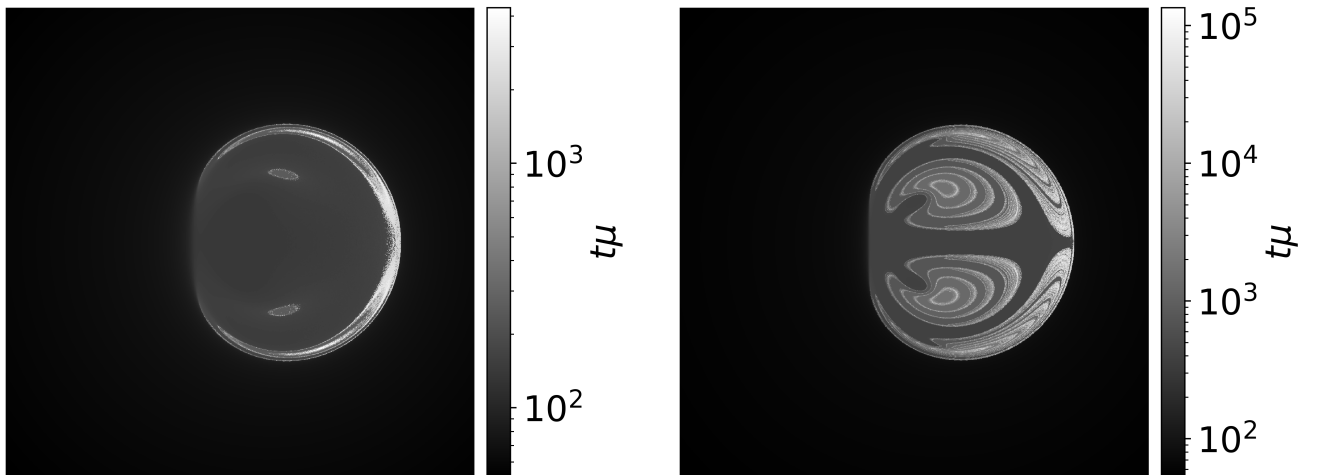


Figure 5: Time delay map associated to scattering orbits in the PS solutions 12.0 (left) and 13.0 (right). Comparison with the bottom middle and right panels of Fig. 4 illustrates how the more pixelated (chaotic) image regions correspond to light ray trajectories that require much larger integration times to complete.

Finally, in Table 1 we summarize some key features of the PSs data set by indicating the frequency (in units of μ) of the solution at which they first appear.⁴ For comparison, we also present the same information but for the rotating BSs case [33]. We observe that the emergence of the first light ring precedes that of an ergo-region, which is first spotted at $\omega \simeq 0.602$. This is generic feature: it was recently proved that any stationary, axisymmetric and asymptotically flat spacetime in $1 + 3$ dimensions with an ergo-region must have at least one light ring outside the ergo-region [57]. Thus, some of the PSs solutions that we present here provide another example where the converse statement of the above mentioned theorem does not hold.

The fact that ultracompact spinning PSs do not feature an ergo-region is useful in isolating imprints of the light ring instability from those of ergo-region sourced instabilities - see *e.g.*, [58]. The light ring instability has been suggested to be associated with the presence of stable light rings in the spacetime [55, 59, 60], and ultracompact PSs necessarily have both a stable and an unstable LR [60]. For the case of PSs this instability was recently shown to lead to a migration of the ultracompact PSs to non-ultracompact ones [56].

Family	ω first Einstein ring	ω for Multiple rings	ω of Light rings	ω for ergo-region
Proca	0.90	0.75	0.711	0.602
Scalar	0.92	0.75	0.747	0.658

Table 1: Main features of the PSs and BSs dataset and the corresponding frequencies at which they first emerge.

As a final comment, we remark that the whole analysis of the lensing features by spinning PSs has a clear qualitative parallelism with the analogous study of their scalar cousins [33, 35].

5 Lensing by KBHsPH

Let us now consider the lensing images and shadows of KBHsPH. Here, besides the frequency ω , the solutions are also parameterized by the radial coordinate of the event horizon, r_H . In general, the larger the value of r_H , the smaller is the deviation from Kerr.

Similarly to the scalar case, KBHsPH have Kerr-like shadows near the existence line (whence they bifurcate from Kerr solutions) for the same mass, angular momentum and comparable observation conditions. This is the case for instance of solution 3.4 - Fig. 6 (top left panel). Considering then the sequence of solutions 3. v (with $v \in \{1, 2, 3, 4\}$), one observes a monotonically decreasing shadow size as v also decreases - see Fig. 6 (top panels, from left to right). The decreasing shadow size seems a natural consequence of the correspondingly smaller fraction of the horizon mass to the ADM mass. We remark that the sequence of KBHsPH solutions 3. v bifurcate from the PS solution 3.0, with frequency $\omega^{3.0} = 0.95$.

⁴Some of this information was recently reported in [56].

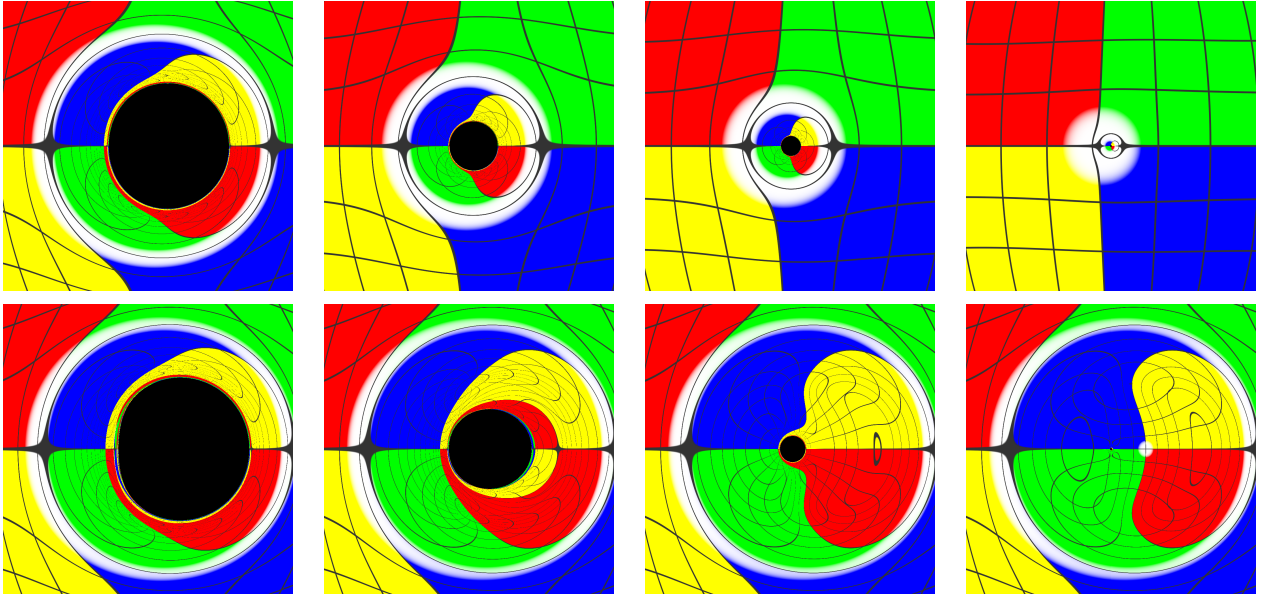


Figure 6: Subsets $\omega^{3.4,3.3,3.2,3.1} = 0.95$ (top) and $\omega^{6.4,6.3,6.2,6.1} = 0.80$ (bottom) of KBHsPH solutions. The value of the horizon mass decreases from left to right.

We can consider next the sequence of solutions $6.v$, with $v \in \{1, 2, 3, 4\}$ - see Fig. 6 (bottom panels), which bifurcates from a Kerr solution at a higher spin. This manifests in the shadow of solution 6.4 having a slightly more D -like shape (a distinctive feature of a spinning Kerr observed from the equatorial plane), at least in comparison to solution 3.4 in the previous sequence - see bottom left panel of Fig. 6.

Another curious feature, apparent along the sequence $6.v$, is the (approximately) composite nature of these hairy BHs, *i.e.* the lensing effects are akin to what one would expect of an horizon in the center of a PS. In particular, for the solution 6.1, the bosonic part clearly dominates the geometry, and the lensing image closely resembles that of the PS solution 6.0 analyzed in the previous section - Fig. 3 (bottom middle panel).

Clear non-Kerr features emerge in the sequences with smaller frequency ω , for instance in the subsets $7.v$ and $8.v$ (cf. Fig. 7), as well as $9.v$ and $10.v$ (cf. Fig. 8), where $v \in \{1, 2, 3\}$. An example of such non Kerr-like features are peculiar “egg-like” shadow shapes, *e.g.* 7.3 and 8.2 - respectively top-left and bottom-middle panel of Fig. 7. Another notable image characteristic is for example the existence of a “cuspy” shadow edge ⁵, *e.g.* 8.3 and 10.3 - bottom left panel of respectively Fig. 7 and Fig. 8.

Some of these image features can be connected to a complex FPO structure. For instance, solution 8.3 has two additional light ring orbits with respect to Kerr, one of them being stable. This is consistent with the PS limit solution 8.0, that has two light rings (one stable and another unstable). Solution 8.3 contrasts with some of the other KBHsPH solutions already discussed, *e.g.* the sequence $6.v$, which (like Kerr) only possessed two light rings, both of them unstable.

In the next section we shall attempt to explain some of these features by an in-depth analysis of the FPO structure of these solutions.

⁵Another study of BHs with cuspy shadows was presented in [61].

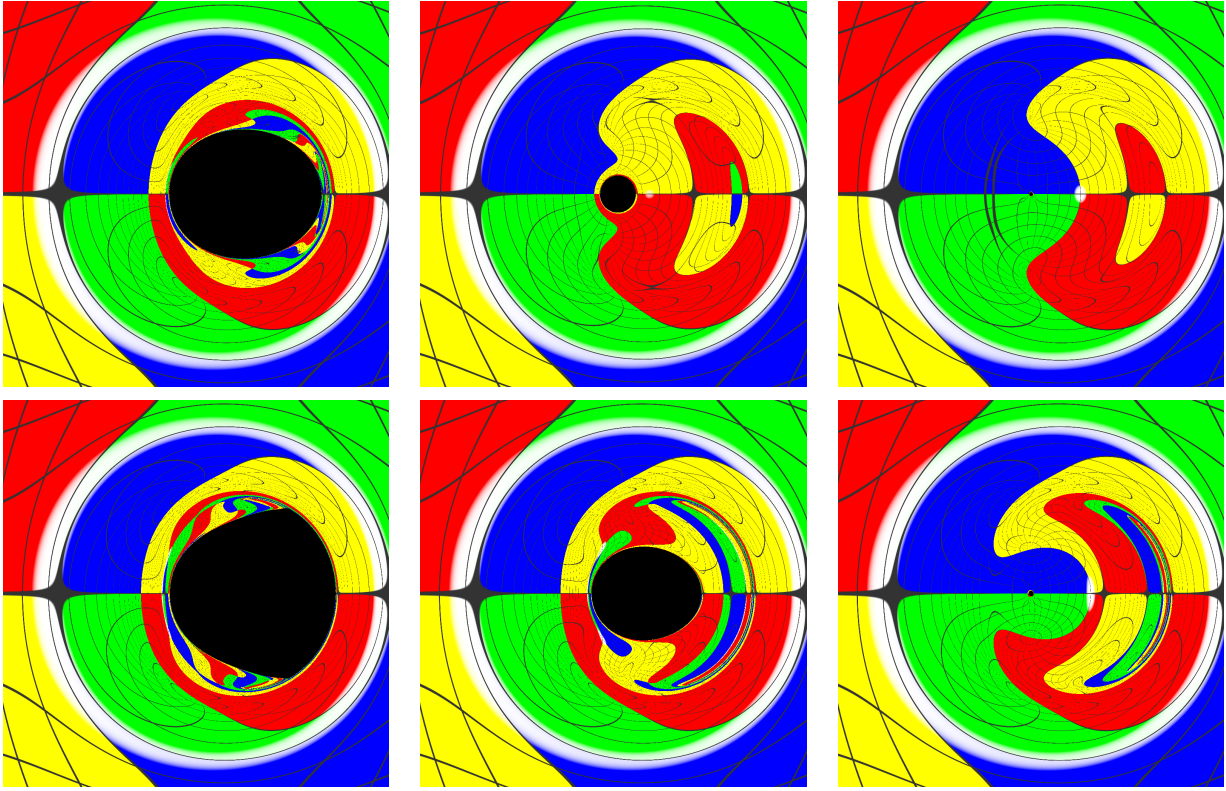


Figure 7: Subsets $\omega^{7.3,7.2,7.11} = 0.75$ (top) and $\omega^{8.3,8.2,8.1} = 0.70$ (bottom) of KBHsPH solutions. The value of the horizon mass decreases from left to right.

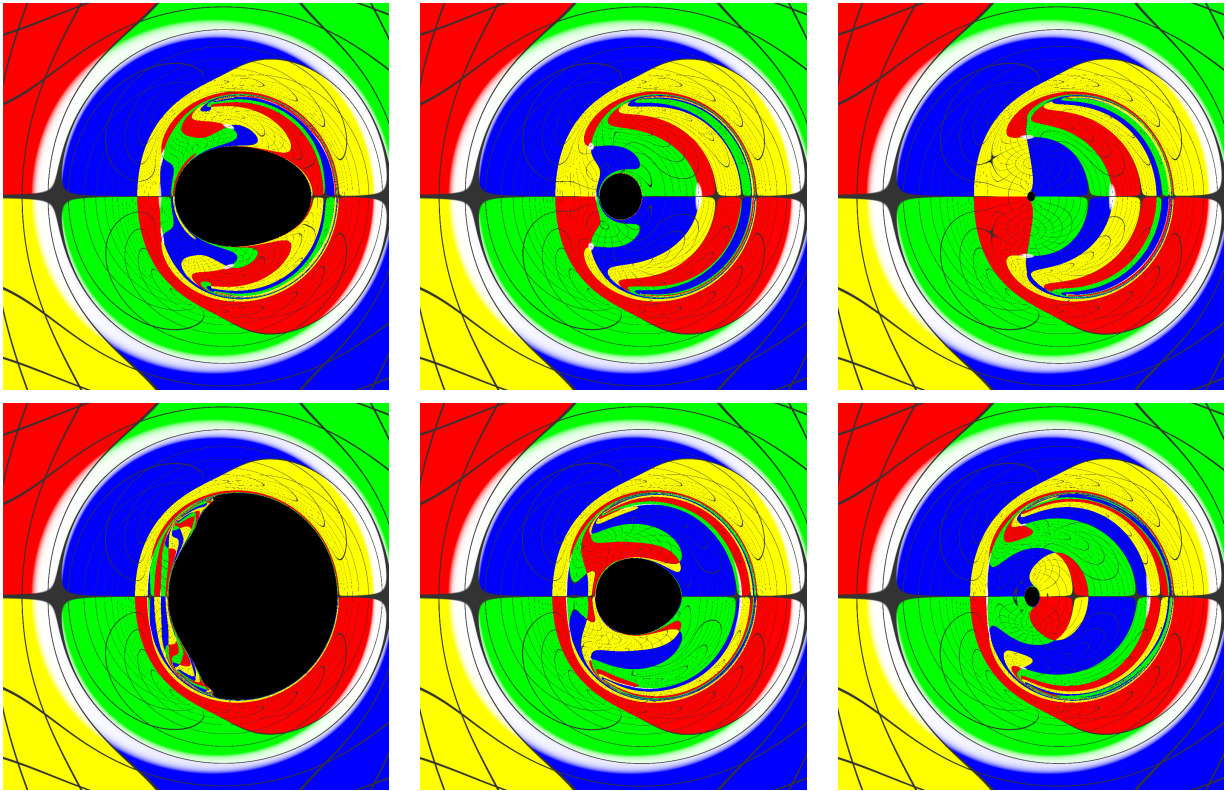


Figure 8: Subsets $\omega^{9.3,9.2,9.1} = 0.65$ (top) and $\omega^{10.3,10.2,10.1} = 0.60$ (bottom) of KBHsPH solutions. The value of the horizon mass decreases from left to right.

6 Fundamental photon orbits

6.1 Overview

In the Kerr spacetime, the edge of the BH shadow is closely related to the notion of SPOs [6, 8]. More specifically, points along the shadow edge define the necessary initial condition for null geodesics to asymptotically approach SPOs, which are unstable bound orbits of constant (Boyer-Lindquist) radial coordinate. Light rings in particular are a subset of these SPOs - the planar ones - and define the two shadow points on the equator, in the case of observations at $\theta = \pi/2$.

In more general spacetimes, such as the ones discussed in this paper, the concept of SPOs can be generalized. However, the condition $r = \text{const.}$ is not geometrically invariant, since it is not preserved by coordinate mixing of r and θ . In addition, typically there is no key property that singles out a particular coordinate chart, such as the geodesic separability that exist in the Kerr case for Boyer-Lindquist coordinates [9].

Nevertheless, the concept of FPOs has been introduced in [9], which generalizes SPOs and include the latter as a subset. Although its definition is more general, in the specific metric ansatz (3) a FPO is simply a null geodesic that describes a periodic trajectory when projected in (r, θ) space.

The dynamics of the null geodesic flow can be derived from the Hamiltonian $\mathcal{H} = \frac{1}{2}g^{\mu\nu}p_\mu p_\nu = 0$, where p_μ is the photon's 4-momentum. In terms of the first integrals $p_t \equiv -E$ and $\Phi \equiv p_\phi$, we can define an effective potential $V(r, \theta)$ and a kinetic term $T \geq 0$ such that $2\mathcal{H} = T + V$. In particular we have

$$T = g^{rr}p_r^2 + g^{\theta\theta}p_\theta^2 \geq 0, \quad (7)$$

and

$$V = g^{tt}E^2 - 2g^{t\phi}E\Phi + g^{\phi\phi}\Phi^2 \leq 0. \quad (8)$$

Given that the kinetic term T is never negative, from the equation above we conclude the boundary for the allowed region in (r, θ) -space is given by the condition $V = 0$. Each FPO is confined to its own allowed region, which depends on the value selected for the impact parameter $\eta \equiv \Phi/E$.

We will follow the classification of FPOs proposed in [9], as follows: FPOs are identified by a symbol $X_{n_s}^{n_r \pm}$, where $X = \{O, C\}$, and $n_r, n_s \in \mathbb{N}_0$, such that:

1. $X = O$ (C) if the orbit is open (closed);
2. A plus (minus) sign is used if the orbit is even (odd) under the \mathbb{Z}_2 reflection symmetry around the equatorial plane;
3. n_r is the number of times that the orbit crosses the equatorial plane;
4. n_s is the number of self-intersection points.

In addition, FPOs can be classified according to their stability under small trajectory perturbations. In Kerr spacetime all FPOs outside the horizon are unstable but, as discussed in [9], this not always true for other spacetimes.

Although the SPOs of the Kerr spacetime allow for very intricate motion around the BH (as thoroughly discussed in [8]), all of them can be classified as either \mathcal{O}_0^{0+} (for light rings) or \mathcal{O}_0^{1+} . As

we will see in the next section, this scenario changes drastically when we consider KBHsPH. In Fig. 9 we provide an example of all the classes of FPOs that we discuss in this paper (with the exception of light rings). The existence of some of these *exotic* FPOs have already been reported. For instance, FPOs of type \mathcal{O}_0^{0+} that are not light rings have been found in Kerr BHs with scalar hair [35], whilst some FPOs with more than one self-intersection where known to be possible for some PS models [9].

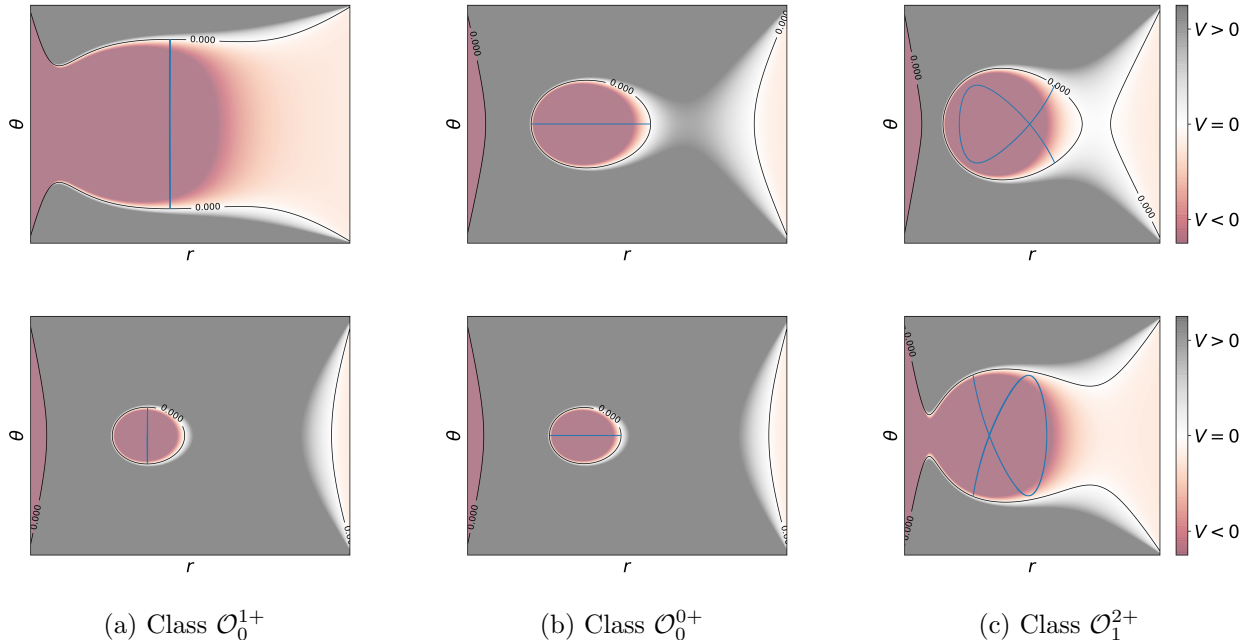


Figure 9: Representation, in the (r, θ) plane, of the FPOs classes featured in the paper. The heat map represents to the values taken by the effective potential $V(r, \theta)$.

In the following sections we address, in a more systematic way, how these different FPOs classes emerge within the space of solutions, while also arguing for a close connection with the features seen in the lensing images discussed previously.

6.2 Analyzing lensing images using FPOs

Kerr BHs possess two light rings with opposite rotation senses, both of them unstable: one for a negative impact parameter, η_-^{LR} , and another for a positive one, η_+^{LR} . A continuum family of SPOs exists between the two light rings, with $\eta_-^{LR} \leq \eta \leq \eta_+^{LR}$, all of them related to one or more points of the shadow edge (see [9]).

We represent in Fig. 10 the SPO family for an extremal Kerr BH in terms of the impact parameter η and the corresponding Boyer-Lindquist radius coordinate r . Critically, each individual SPO (which is also an FPO) is uniquely labelled by its radial coordinate at the crossing point with the equatorial plane.

A similar method can be used to label FPOs around KBHsPH, provided that the FPOs intersect the equator. Such a labelling criteria is necessary because FPOs around KBHsPH will no longer be described (generically) by a single radial coordinate along its trajectory. The radial coordinate of the FPO at the equatorial plane crossing point is a geometrically well-defined choice, since that point is invariant under the \mathbb{Z}_2 reflection symmetry.

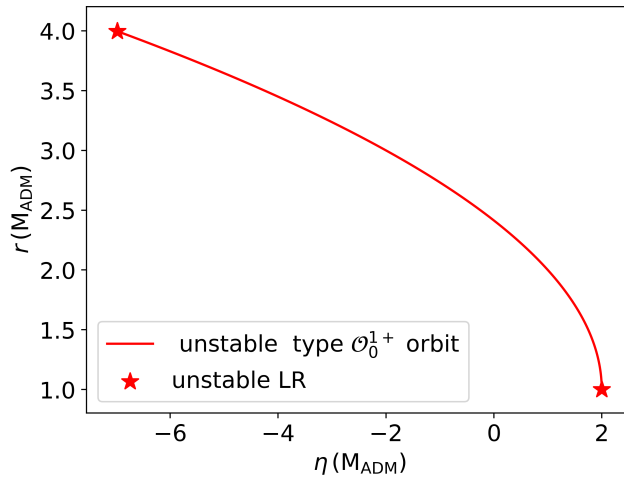


Figure 10: Diagram of the FPO family of an extremal Kerr BH.

It is not unexpected that there exists a subset of hairy BH solutions whose FPO family structure does not differ very much from the Kerr case. For the specific examples we discussed above, in terms of the lensing, this is the case for solutions with frequencies down to $\omega^{7.v} = 0.75$. Below this frequency we find lensing images with distinctively non-Kerr shadow features that can be connected to distinctive FPO structures, as we now discuss.

Cuspy shadow

As we progress to smaller frequencies, solution 8.3 (with $\omega^{8.3} = 0.70$) is one of the first whose shadow displays some striking deviations from Kerr - Fig. 7 (bottom left panel). In [9], the authors also analysed a hairy BH solution with a cusp on the shadow edge, and then related this feature to the existence of two (discontinuous) different FPO branches related to the shadow edge. Although the solution studied in [9] corresponds to a different family of hairy BHs solutions⁶, we verified that the same interpretation of the shadow cusp also applies here, as we shall now discuss, reinforcing the idea that FPOs are a useful non-trivial tool when it comes to understanding non-Kerr features present in shadows and lensing images.

In Fig. 11 we present the FPO family diagram for solution 8.3, where it is clear that there are two distinct and discontinuous branches of unstable FPOs that are shadow related - the red and yellow solid lines. The red line is dubbed the *lower* branch, occurring for larger (albeit some still negative) impact parameters, whereas the yellow line is dubbed the *upper* branch, occurring for smaller (and all negative) impact parameters. These two branches actually connect to each other via some other FPOs that are not shadow related, some being stable and others unstable. Each branch of the shadow related FPOs terminates at a light ring, on one end, and at a particular FPO, on the other end. The impact parameter of the latter is the same for both branches, which allows the shadow edge to be continuous, but not smooth (as a curve). This explains the cusp seen in the shadow edge of solution 8.3, which is displayed in Fig. 12 together with an illustration of how each shadow point is mapped to a corresponding FPO branch.

⁶The solution analyzed in [9] is an example of an excited KBHPH, rather than fundamental as the ones discussed here.

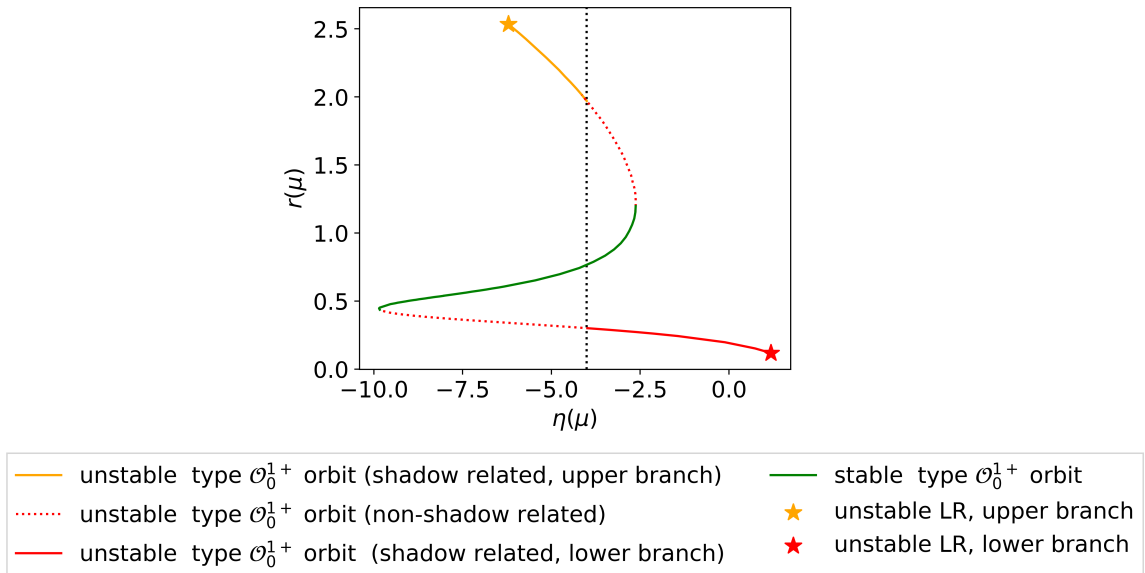


Figure 11: FPO family diagram for solution 8.3. The black dotted line marks the separation between the two FPO branches related to the shadow edge.

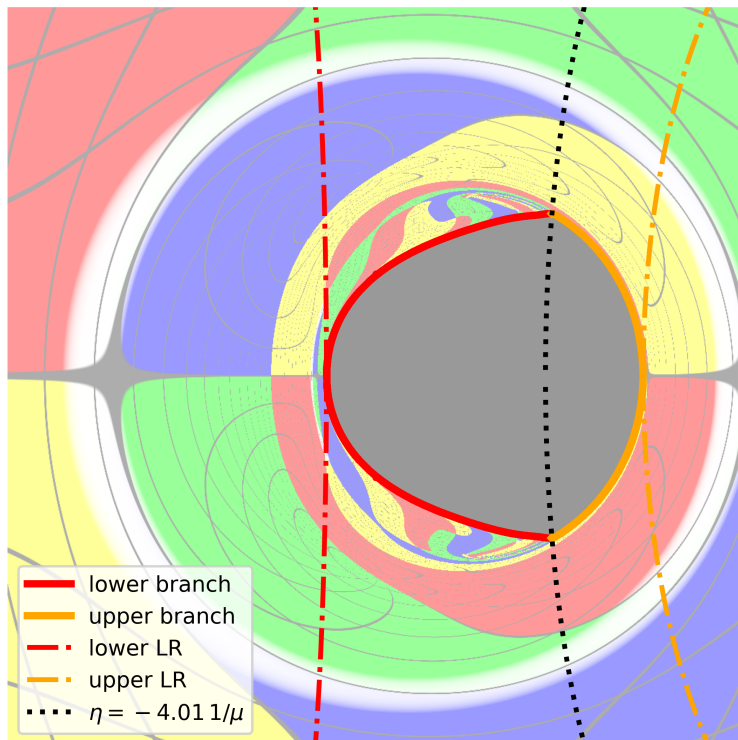


Figure 12: Different sections of the shadow contour of solution 8.3, connected to distinct FPO branches, are represented by solid lines. In addition, points in the image with constant impact parameter η are displayed by either dotted or dotted-dashed lines. The impact parameter $\eta = -4.01/\mu$ marks the separation between the two FPO branches, and corresponds to the vertical dotted line shown in Figure 11. Dotted-dashed lines with the impact parameter of both light rings (LRs) are displayed for reference, intersecting the shadow edge at the points determined by the light ring orbits.

Curiously, solution 8.3 is also fairly close in the domain of existence of KBHsPH to solution 8.2, which has two additional light rings (one stable and the other unstable) with respect to 8.3 - see Fig. 1.

This realization, together with an examination on how extra light rings might emerge by deforming the FPO family diagram (see also the discussion of the next section), leads to the conjecture that the presence of a cuspy shadow could signal the near-emergence of a second pair of light rings in the space of solutions. It would be interesting to further explore this idea on general grounds.

Ghost shadows

In Fig. 13 we present the FPO family diagram for solution 8.2, which contains four light rings in total. The lensing image of this solution can be found in Fig. 7 (bottom middle panel). With the emergence of the second light ring pair, we now have two fully disconnected branches: the shadow related branch (the lower branch, which completely defines the shadow edge, therefore being smooth with no cusp) and a non-shadow related branch (the upper one).

This upper branch can be divided into three different sub-branches: a stable⁷ and unstable \mathcal{O}_0^{1+} type orbits and a stable \mathcal{O}_0^{0+} type one.

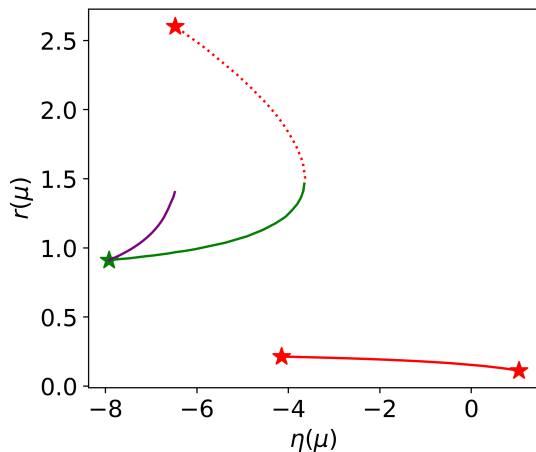


Figure 13: FPO branch diagram for solution 8.2. Since orbits of type \mathcal{O}_0^{0+} do not exit the equatorial plane, the radius used to represent these orbits corresponds to the radial mean value.

Orbits of type \mathcal{O}_0^{0+} discussed here are restricted to the equatorial plane and, thus, there are several available options when it comes to labelling these orbits with a single coordinate r value. In this paper, the radial value used to represent type \mathcal{O}_0^{0+} orbits corresponds to the mean radial value, defined as the average of the maximum and minimum r values reached along the geodesic motion. By labelling these FPOs in such a manner, the \mathcal{O}_0^{0+} branch upper end point in Fig. 13, *i.e.* with largest radius, coincides precisely with the radius at which the the stable \mathcal{O}_0^{1+} branch connects to the unstable one.

In [9] the authors discussed how unstable FPOs non-related to the shadow could be associated to a set of lensing patterns attached to the shadow edge, dubbed "eyelashes". A similar feature can be seen in the lensing of 8.3 (cf. Fig. 7, lower left panel). After the emergence of a second pair of light rings in solution 8.2, the eyelashes appear to become disconnected from the shadow, forming a pixelated banana-shaped strip that can be seen in the lensing image - see bottom middle panel of Fig.

⁷Note that stable branches never contribute to the shadow edge.

7. This feature has been dubbed “ghost shadow” in the literature [62], and it seems plausible that it is a consequence of the existence of the unstable FPO branch that is non-related to the shadow. This question merits a rigorous formulation and analysis which is, however, outside the scope of this paper.

Shifting our attention to solution 9.3 (Fig. 8, top left panel), FPOs of type \mathcal{O}_1^{2+} can also be found (cf. Fig. 14). These orbits were already reported to exist in PSs [9], but it was still unknown whether they could be present in KBHsPH, and how they were related to the other FPOs branches. In Fig. 14 we see that \mathcal{O}_1^{2+} FPOs (blue line) bifurcate from the already familiar \mathcal{O}_0^{1+} stable branch (the green line). We verified that the \mathcal{O}_0^{1+} branch separates the new \mathcal{O}_1^{2+} into two sub-classes: the two different orientations shown in Figure 9b. Since these are stable FPOs, it is not possible to establish a direct link between them and the shadow image. Nonetheless, it might be interesting to study these FPOs on a mathematical level: in particular, it is not evident what is special about the bifurcation point at which these FPOs emerge in the family diagram. It remains an open problem whether the emergence of these different FPOs can be associated to conserved topological quantities, in a similar spirit to the topological charge associated to the existence of light rings [60, 63],

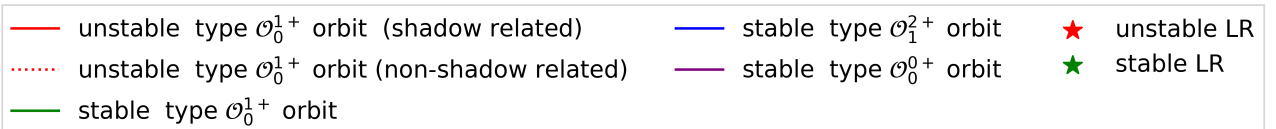
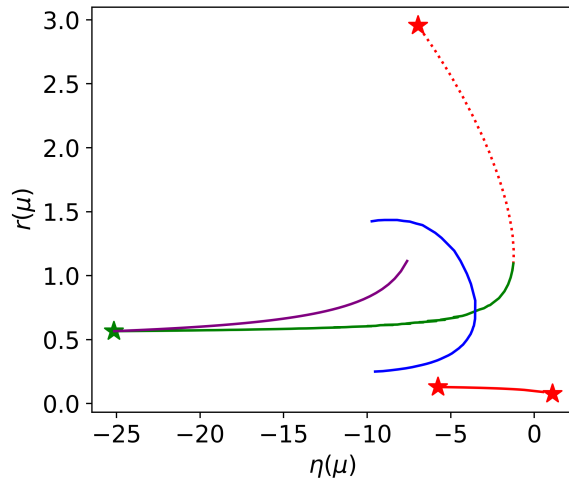


Figure 14: FPO branch diagram for solution 9.3.

Additional FPOs classes, other than the ones discussed in this paper, might still be present in the solutions that we discuss here. The numerical analysis implemented in this work focused on FPOs that crossed the equatorial plane perpendicularly at least once. If other FPOs that do not verify this condition were to be present, then they would have been overlooked by the analysis herein.

7 Analyzing the astrophysically viable space of solutions

In the previous sections we have been addressing theoretical aspects of the lensing and shadows of KBHsPH and their solitonic limit, PSs. We have focused, in particular, on distinctively non-Kerr features, to clearly exhibit the exoticness that can occur in this model. We would now like to consider the potential observability of this model via current or near future observations. As such, hereafter

we shall focus on the solutions that are astrophysically viable, in the sense that a plausible formation mechanism exists. As discussed in [36], these are solutions that one can expect to be formed from a Kerr BH via superradiance (see also [64] for hairiness limit of such solutions), and whose superradiant instabilities are only relevant on very long, possibly cosmological, time scales [65].

In Fig. 15 we display the part of the domain of existence containing the solutions that we have considered for the observability study. It comprises solutions for which $0.1 \leq M\mu \leq 0.6$. Only a subset of these solutions might actually be formed through superradiance, depending on their fraction of hair p . The latter is defined as the ratio between the (Komar) mass of the BH horizon M_{BH} to the total mass of the spacetime M :

$$p \equiv 1 - \frac{M_{BH}}{M} . \quad (9)$$

Fully dynamical numerical evolutions of the superradiant instability around a Kerr BH, driven by a complex vector field, were shown to form KBHsPH with $p \lesssim 0.1$ (see [19, 23, 24] for details). As discussed in [64], the bound $p \lesssim 0.1$ can be expected to hold in general regardless of the spin of the bosonic field, as long as the development of the superradiant instability from Kerr is assumed to be approximately conservative. Numerical evolutions have indeed suggested the latter to be the case, at least in the cases studied thus far [23, 64]. Nevertheless, even if such an assumption were not to hold, there is an overall thermodynamic bound on the maximum rotational energy that can be extracted from Kerr, setting a conservative upper limit of $p \lesssim 0.29$.

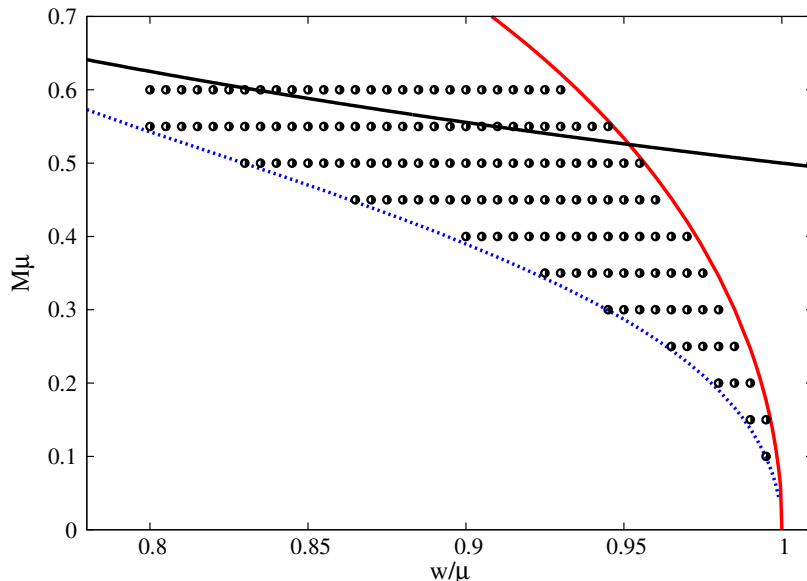


Figure 15: Domain of existence of the astrophysically viable solutions. This is a sub-region of Fig.1. As in that figure, the red solid line is the PS limit and the blue dotted line is the Kerr limit. The black solid line is the extremal Kerr line. The black dots highlight the solutions used in our analysis of this and the following sections.

For a wider analysis, the region represented in Fig. 15 also includes solutions that do not verify the condition $p < 0.1$ (or even $p < 0.29$). Such solutions are also valid equilibrium solutions of the Einstein-Proca system of equations, and one cannot dismiss the possibility of formation by alternative channels other than the growth of the superradiant instability - see *e.g.* [66]. Moreover, the inclusion

of solutions with $p > 0.1$ allow us to have a better interpolation sample for the shadow size throughout the solution domain.

In order to make contact with the observational data we shall work with a simple measure of the BH shadow size: the areal radius S , defined as

$$S \equiv \sqrt{\frac{\mathcal{A}}{\pi}}, \quad (10)$$

where \mathcal{A} is the area of the shadow, which in general depends on the distance and inclination of the observer with respect to the BH. The areal radius can then be related to the angular size ϑ of the BH shadow, which is measured by the EHT observations. For a BH with mass M , located at a perimetral distance \mathcal{R} from the observer, the relation between ϑ and S is provided via the expression

$$\vartheta = (S/M) \frac{M}{\mathcal{R}}. \quad (11)$$

Both EHT observations of M87* and Sgr A* are, so far, consistent with the Kerr metric within the current uncertainty level of $\simeq 10\%$ of the shadow angular size [12, 67]. However, having such a (fairly) large uncertainty in the shadow size measurement leaves the door open to alternative Kerr models that also might be consistent with observations, namely KBHsPH. This possibility raises the interesting question of how much Proca hair might exist outside the horizon, provided that its shadow is still consistent with the EHT observations and their uncertainties. In the remainder of the paper we shall focus on this issue by analysing how much the areal radius of KBHsPH shadows deviate from Kerr as function of the amount of hair, p , and the parameter $M\mu$. For this deviation analysis we shall compare the shadow of each hairy BH solution with the one from a comparable Kerr BH of equal mass $M\mu$, lying along the Kerr existence line in the KBHsPH solution space. Thus, it is convenient to express the Kerr dimensionless spin parameter, a , as function of $M\mu$.

Along the Kerr existence line, the spin parameter a is related to the angular velocity at the horizon, Ω_H via:

$$a = \frac{M^2 \Omega_H}{M^2 \Omega_H^2 + 1/4}. \quad (12)$$

Then, the data in Fig. 15 allow us to write an approximation for the function $M\Omega_H(M\mu)$:

$$M\Omega_H \approx b_1 + b_2 M\mu + b_3 M^2 \mu^2, \quad (13)$$

with $(b_1, b_2, b_3) = (-0.00938981, 1.16616021, -0.63782197)$. By combining equations (12) and (13) one can directly describe the spin of the comparable Kerr BH solutions mentioned above.

8 Constraining the hair using M87* data

8.1 Approximation formula for the shadow viewed from 17° inclination

Although it is possible to obtain numerically the shadow size of KBHsPH up to a fairly high precision, it will become useful in the following sections to work with an analytical approximation instead.

Following [36], we start by expressing the Kerr areal radius as a function of the spin and of the polar angle of the observer, θ_o . This can be achieved by interpolating between the two cases where the shadow area can be computed exactly: when the observer is on the rotation axis (*i.e.*, $\theta_o = \{0, \pi\}$), and for the case of an extremal Kerr BH viewed from the equatorial plane in the far-away limit. The resulting expression can be written as [36]:

$$S_{\text{Kerr}}(a, \theta_o) \approx S_{\text{Kerr}}(a, \text{axis}) + \frac{2|a|\theta_o}{\pi M} \left[S_{\text{Kerr}}\left(M, \frac{\pi}{2}\right) - S_{\text{Kerr}}(M, \text{axis}) \right], \quad (14)$$

which gives an error $\lesssim 0.8\%$.

Since KBHsPH shadows are obtained numerically with the observer at a finite (perimetral) distance from the BH, their size cannot be immediately compared with the Kerr analytical approximation (14), which is constructed for observers at infinity. Following [36], this issue is addressed by i) considering how the numerical shadow size S changes among two observers, respectively $\{S_1, S_2\}$, at large (finite) perimetral distances $\{\mathcal{R}_1, \mathcal{R}_2\} \gg M$, and then ii) by extrapolating the value of S to the limit of an infinitely far-away observer. This procedure leads to:

$$S_\infty \approx S_2 - \left(\frac{S_2 - S_1}{1 - \mathcal{R}_1/\mathcal{R}_2} \right). \quad (15)$$

In our analysis we considered the values $\mathcal{R}_1 = 100M$ and $\mathcal{R}_2 = 200M$.

In order to describe the KBHsPH areal radius at infinity as viewed from an observer at $\theta_o = 17^\circ$ (which corresponds to the angle between M87* BH spin and the line of sight [68]), we propose the following approximation formula:

$$S_{\text{hairy}}(p, M\mu, 17^\circ)/M = (1-p) \left[S_{\text{Kerr}}(a(M\mu), 17^\circ)/M + \sum_{i=0}^2 \sum_{j=0}^4 \alpha_{ij} (M\mu)^j p^{i+1} \right], \quad (16)$$

The parameters α_{ij} used for the fit can be found in the matrix Table 2 below.

$$\begin{pmatrix} \alpha_{00} & \alpha_{01} & \cdots \\ \alpha_{10} & \ddots & \\ \vdots & & \ddots \end{pmatrix} \equiv \begin{pmatrix} -1.266 & 18.821 & -90.696 & 267.305 & -236.951 \\ 4.741 & -68.491 & 388.415 & -1066.683 & 1063.879 \\ 5.535 & -66.439 & 226.226 & -152.9 & -225.308 \end{pmatrix}$$

Table 2: Values for the parameters α_{ij} for an observer at $\theta = 17^\circ$.

The approximation (16) has an average error of 1.1% when all the solution points represented in Fig. 15 are considered. However, solutions of particular interest will be the ones that might grow from Kerr BHs via superradiance, which form a solution subset with restricted values of p . By restricting ourselves to solutions satisfying the more conservative thermodynamic upper limit of $p \lesssim 0.29$, then eq. (16) has an error smaller than 0.8% overall, and around 0.14% in average.

The accuracy of this approximation can also be inferred from Fig. 16, where we show the areal radius for hairy BHs computed via ray-tracing and the function $S_{\text{hairy}}(p, M\mu, 17^\circ)/M$.

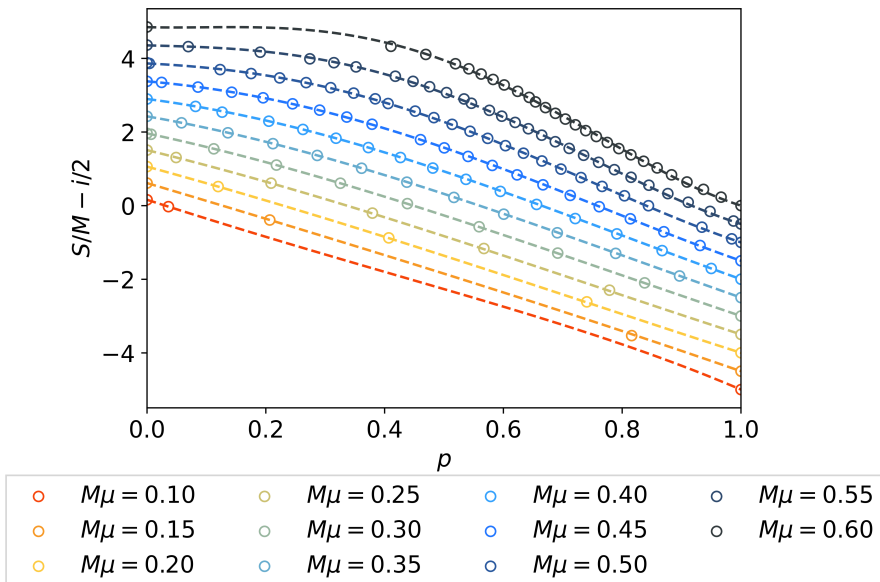


Figure 16: Areal radius for hairy BHs (dots) and the analytical approximation (dashed lines) 16. Each line correspond to a constant $M\mu$ value and, to better distinguish them, they are translated by an amount $-i/2$, where $i = \{0, \dots, 10\}$.

8.2 Application to the M87* BH shadow

Using Eq. (16), we can now easily inspect how the shadow of KBHsPH deviates from that of the comparable Kerr BH by introducing the deviation δS :

$$\delta S(p, M\mu) \equiv 1 - \frac{S_{\text{hairy}}(p, M\mu, 17^\circ)}{S_{\text{Kerr}(a(M\mu), 17^\circ)}}. \quad (17)$$

In Fig. 17 we represent how the deviation $\delta S(p, M\mu)$ changes as a function of the amount of hair p , for a selection of $M\mu$ values. The profile of δS as a function of p depends strongly on the value of $M\mu$ being considered. This comes in sharp contrast with the scalar case discussed in [36], in which case the deviation was roughly proportional to the fractional amount of hair, regardless of $M\mu$. However, for KBHsPH this is only true for smaller $M\mu$ values.

Focusing on the solutions with $p \lesssim 0.1$ - the ones that may grow from a Kerr BH via its superradiant instability and are therefore dynamically plausible through this formation channel - then all such solutions are still compatible with the EHT M87* constraint, as in the scalar case. Nonetheless, by considering the possibility that hairier BHs can still be formed via other dynamical channels, such as the merger of bosonic stars [69], one faces the interesting prospect that very hairy BHs with sufficiently large $M\mu$ (up to $p \simeq 0.4$ in the data considered) could be mistaken by a Kerr BH with the current observational data.

The main implication of this shadow analysis is that the vector (Proca) case introduces a more complex picture than that of the scalar case, described in [36]. For instance, as one can realise from Fig. 17, KBHsPH can in fact become better Kerr mimickers, since there are solutions whose shadow deviation from the comparable Kerr is below 10% and that possess up to 40% of the total mass stored on the Proca hair outside the horizon (*i.e.* $p = 0.4$). It is nothing short of surprising that having such

a significant deviation on the spacetime geometry can still lead to small deviations on shadow size. This scenario contrasts with the scalar case, wherein a shadow deviation of 10% disfavoured solutions with $p > 0.1$. This is a key difference that we have unveiled between the two models. We will come back to this difference and its possible cause below.

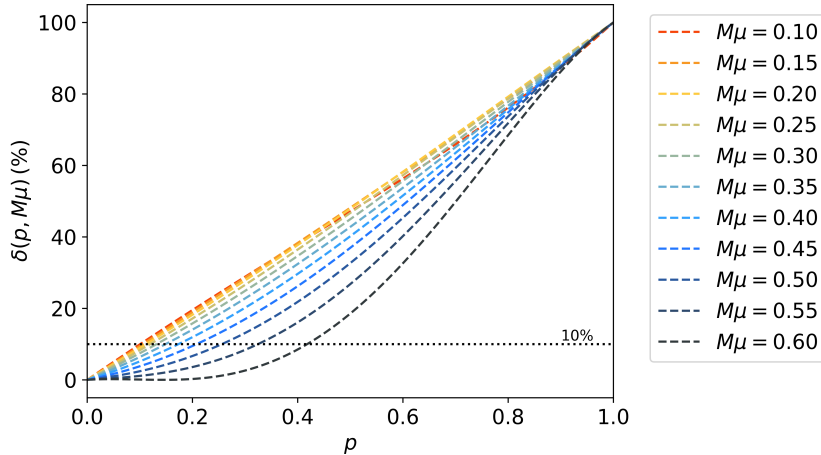


Figure 17: Deviation from Kerr as function of hairiness for the different $M\mu$ considered. The horizontal dotted line corresponds to a deviation of 10%, which sets an approximate upper threshold for consistency with the EHT observations of M87*.

According to Fig. 17, for a fixed $M\mu$, the greater the value of p , the greater is the deviation δS . Thus, each value of p determines a minimum observation resolution necessary to test that KBHPH model, for a given $M\mu$. This is clear by looking at the left panel of Fig. 18, where we represent $\delta S(p, M\mu)$ as function of $M\mu$ for fixed values of p from 0.1 to 0.29. From this plot we realise that as we increase $M\mu$, and for a fixed p , the more challenging it becomes to distinguish a KBHsPH solution from a Kerr one.

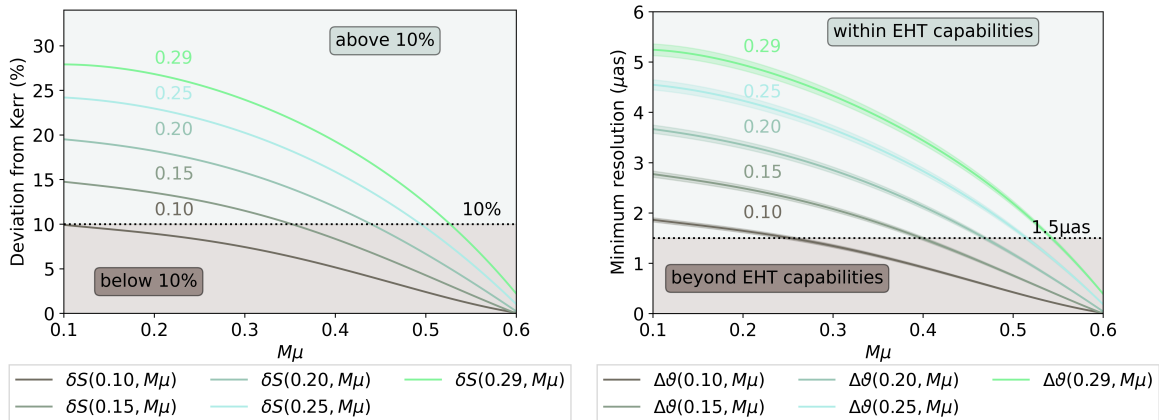


Figure 18: On the left panel the shadow deviation from Kerr is represented as function of $M\mu$ for different fixed values of fractional hair p . The right panel features a similar diagram, albeit with the minimum M87* angular resolution required to test the model as function of $M\mu$, where the shaded bands account for the uncertainty in the M87* known distance and mass.

This degeneracy demands more than our current observational capabilities to rule out the hypothesis that the BHs that we observe are in fact BHs with synchronized Proca hair, at least considering

formation from superradiance under the theoretical (thermodynamical) upper limit of $p \simeq 0.29$ [64, 70]. The necessary optical resolution to test these models can be obtained from the relation between the shadow areal radius and its angular size via Eq. (11), which requires knowledge of the mass-distance ratio $\lambda = M/\mathcal{R}$ from M87* to Earth. This ratio λ can be inferred from two independent measurements – one based on star dynamics (hereafter “star data”) [71], and another one based on gas motion (hereafter “gas data”) [72]:

$$\begin{cases} \lambda_{\text{star}} = 0.369 \pm 0.022 \left(\frac{10^9 M_{\odot}}{\text{Mpc}} \right) \\ \lambda_{\text{gas}} = 0.196^{+0.05}_{-0.04} \left(\frac{10^9 M_{\odot}}{\text{Mpc}} \right) \end{cases} . \quad (18)$$

We shall refer primarily to the star data in our analysis, since gas data is reported to be under tension *even* with the Kerr BH hypothesis [14]. Using the experimental values for λ , we can infer how much the angular shadow size of a KBHsPH solution varies from a comparable Kerr solution, as function of $M\mu$:

$$\Delta\vartheta(p, M\mu) = \lambda \frac{S_{\text{hairly}}(p, M\mu, 17^\circ) - S_{\text{Kerr}}(a(M\mu))}{M} . \quad (19)$$

We represent this quantity, for $p = \{0.1, 0.15, 0.2, 0.25, 0.29\}$, in the right panel of Fig. 18, where we have used the star data. Knowing that the current EHT resolution for the observation of the M87* BH is about $1.5 \mu\text{as}$, this figure tells us how much we need to improve the resolution to fully test our model.

We shall end this section with a more comprehensive and systematic analysis of the parameter region that provides an angular shadow size ϑ compatible with the EHT observation ⁸

$$\vartheta_{\text{M87*}} = (18.9 \pm 1.5) \mu\text{as} . \quad (20)$$

Equation (11) can be first recast in the form $\vartheta(p, \lambda, M\mu) = \lambda S_{\text{hairly}}(p, M\mu, 17^\circ)/M$. Then, for fixed values of $M\mu$, one can scan points in the (p, λ) plane such that both ϑ and λ fall within the observation error-bars of both λ_{star} and $\vartheta_{\text{M87*}}$. The error bars can correspond to some multiple of the respective standard deviation σ of the measured data, for example 1σ or 3σ .

The result of this analysis is displayed in Fig. 19 for both star data (left panel, and within 1σ) and gas data (right panel, and within 3σ). As one could already expect from Fig. 17, and in comparison with the scalar case, there is a much broader range of p values that are still consistent with the EHT data. For instance, if one takes the star data, it is possible to find solutions with $p \gtrsim 0.27$ that are still compatible with the angular size measured with EHT within one standard deviation, for sufficiently large $M\mu$. That is in strike contrast with the scalar case, where one could only get up to $p \approx 0.1$.

⁸This value was determined by assuming that the shadow diameter is 10% smaller than the emission ring diameter reported by EHT (in agreement with [14]). Although we use the same uncertainty as the one associated with the measurement of the ring, it would be more realistic to expect a slightly larger uncertainty for the shadow diameter (as discussed more thoroughly for the case of Sgr A* [18]).

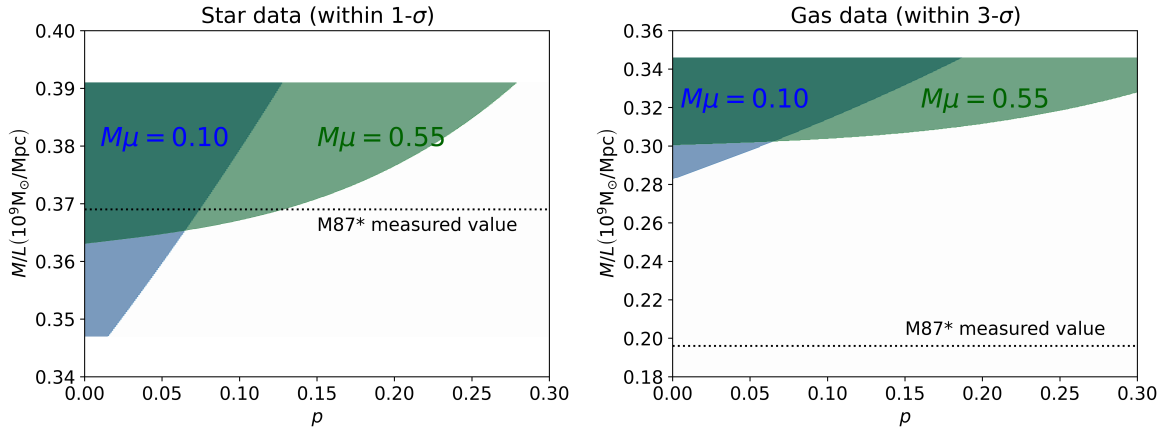


Figure 19: Shaded domains of $(p, \lambda = M/L)$ yield a shadow angular size ϑ consistent with the EHT M87* observation within the uncertainty error-bars of $\{\lambda_{\text{star}}, \vartheta_{\text{M87*}}\}$. Different coloured regions correspond to different values of $M\mu$. Left panel: star data within 1σ ; right panel: gas data within 3σ .

9 Constraining the hair using Sgr A* data

In addition to the M87* analysis of the previous section, we shall perform a similar discussion for the recent EHT observation of Sgr A*, *i.e.* the BH candidate at the centre of the Milky Way [15]. Unlike M87*, the Sgr A* does not feature a clear jet structure from which one can infer the angle between the line of sight and the angular momentum of the BH (*i.e.* the observation (inclination) angle, θ). By assuming different inclination angles, the EHT collaboration concluded that the Sgr A* data disfavors $\theta > 50^\circ$. In addition, as reported in [15], the two GRMHD models that better match the imaging data both have $\theta = 30^\circ$. For this reason, we shall consider in our analysis an observation angle of $\theta = 30^\circ$.

Following the same procedure used in the case of M87*, we have similarly found an approximation formula for the shadow size of KBHsPH using the ansatz in Eq. (16), now with an observation angle of 30° instead of 17° . The corresponding parameters α_{ij} can be found in Table 3.

$$\begin{pmatrix} \alpha_{00} & \alpha_{01} & \cdots \\ \alpha_{10} & \ddots & \\ \vdots & & \ddots \end{pmatrix} \equiv \begin{pmatrix} -1.564 & 22.829 & -112.404 & 321.999 & -290.05 \\ 4.53 & -65.749 & 382.733 & -1093.222 & 1142.351 \\ 5.939 & -73.042 & 258.157 & -198.798 & -236.928 \end{pmatrix}$$

Table 3: Values for the parameters α_{ij} introduced in Eq. (16), for an observer at $\theta = 30^\circ$.

For values of $p \lesssim 0.3$ the formula gives an error smaller than 0.9% overall, and around 0.2% in average. Using this approximation formula for an observation angle of $\theta = 30^\circ$, we have verified that a plot of the deviation of the shadow size from a comparable Kerr leads to a diagram very similar to Fig. 17, without displaying any qualitative differences (plot not shown for conciseness).

The shadow deviation relatively to Kerr does not change significantly by having an observation at a 30° angle rather than 17° . Nevertheless, the EHT observation data of Sgr A* offers us an opportunity to set tighter constraints on the amount of Proca hair that Sgr A* might support, when compared

with M87*. Indeed, the mass-to-distance ratio of Sgr A* has been measured much more precisely than for M87* [18], which allows for a much better estimation of the shadow angular size of KBHsPH.

Following the EHT collaboration, we will base our analysis on two measurements for the mass-to-distance ratio: one by the Very Large Telescope Interferometer (VLTI, [73]), and another by the W. M. Keck Observatory (Keck, [74]). Both values have been measured through the observation of the orbital dynamics of the central stellar cluster around Sgr A* (see [18] for a brief summary). The measured values of the mass-to-distance ratio λ for Sgr A* are given below:⁹

$$\begin{cases} \lambda_{\text{VLTI}} = 5.125 \pm 0.009 \pm 0.020 \text{ } (\mu\text{as}) \\ \lambda_{\text{Keck}} = 4.92 \pm 0.003 \pm 0.01 \text{ } (\mu\text{as}) \end{cases} . \quad (21)$$

In addition, we shall refer to the Sgr A* shadow diameter reported by the EHT [15]:

$$\vartheta_{\text{SgrA}^*} = 48.7 \pm 7.0 \mu\text{as} . \quad (22)$$

Following an analysis similar to the one implemented in Fig. 19, we have displayed in Fig. 20 the region in the plane (p, λ) compatible with the EHT observation of Sgr A* that is still within the observation error-bar of $\{\lambda, \vartheta_{\text{SgrA}^*}\}$. We have considered the VLTI and Keck data separately, one in each of the two plots of Fig. 20. In both cases we are able to find KBHsPH solutions with 30% of the total mass stored in the Proca hair, *i.e.* with $p = 0.3$, and which are still compatible with the EHT shadow observation within 1 standard deviation (1σ).

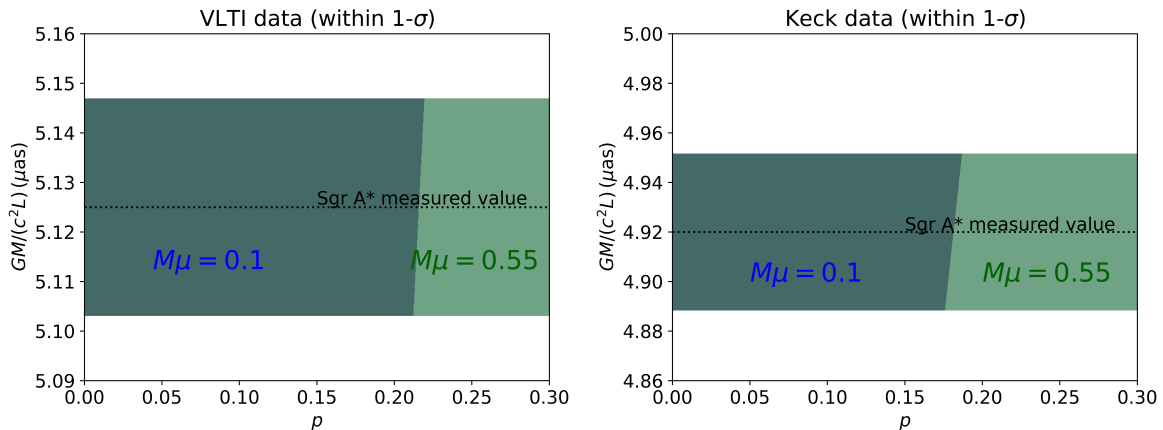


Figure 20: Shaded domains of $(p, \lambda = M/L)$ yield a shadow angular size ϑ consistent with the EHT Sgr A* observation, within the uncertainty error-bars of $\{\lambda, \vartheta_{\text{SgrA}^*}\}$. Different coloured regions correspond to different values of $M\mu$. Left panel: VLTI data within 1σ ; right panel: Keck data within 1σ .

10 Conclusions and Discussion

Research in BH imaging and the optical appearance of BHs has recently become a thriving field, with many studies on how the EHT data can constrain hairy BHs, *e.g.* [75–87] as well as many other academic works on the shadows and lensing by “hairy” spinning (asymptotically flat) BHs - see *e.g.* for some recent studies [88–106] and also the reviews [62, 107].

⁹This quantity corresponds to θ_g , in the notation followed by the EHT collaboration.

In this work we have considered the shadows and lensing of a non-Kerr model – KBHsPH – that is dynamically robust, in the sense that it appears in a sound physical theory with no known pathologies and it has a plausible formation mechanism, as discussed in the Introduction, at least in some regions of the parameter space. Our study has been both academic, exploring the lensing and shadow features across the full domain of existence, as well as phenomenological, focusing on regions of the parameter space where the solutions are astrophysically more plausible (*e.g.* free of stable light rings or FPOs, that can source a spacetime instability).

Our study corroborates the generic expectation: since KBHsPH interpolate between the (vacuum) Kerr solution and the (horizonless) PSs, their lensing features vary from Kerr like – near the former – to very non-Kerr like – for some regions of the parameter space and for solutions with a large fraction of the hair in the Proca field. Concerning the latter, which are more exotic solutions, non-Kerr features such as cuspy, egg-like or ghost shadows emerge typically when the spacetime accommodates a more complex structure of FPOs than Kerr. As emphasised in the text above, it would be interesting to study the generality of some of the features unveiled here, such as: 1) the relation between cuspy shadows and the emergence of new pairs of light rings; or 2) the connection between ghost shadows and the existence of unstable FPOs not-related to the shadow.

Furthermore, the (possibly) most intriguing result from our analysis arose when considering the comparison with observations. Let us contextualize it by recalling the analog result for Kerr BHs with synchronised scalar hair [36]. In this reference it was shown that the scalar hairy BHs were compatible with the EHT M87* measurement up to a fraction of the energy in the hair of the order of 10%. This seems an intuitive result, as this distribution of the energy between the BH and the surrounding environment seems to affect the shadow size by (roughly) 10%, which is of the order of the error in the measurement of the shadow size by the EHT for M87*. Naively, one could have expected a similar result for the KBHsPH discussed here. However, we found that in some regions of the parameter space – and given sufficiently large $M\mu$ –, Proca hairy BHs with at least 29%¹⁰ of their energy in the surrounding environment (rather than in the horizon) are still compatible with the EHT measurement of both M87* and Sgr A*. Our best guess, at the moment, is that the estimation of the variation of the shadow size by the fraction of energy outside the horizon can be misleading, as the shadow is an imprint not of the horizon but rather of the FPOs structure. For reasons that should be better understood this (naive estimate) works well for the scalar hairy BHs, but less for the Proca hairy ones. Thus, it would be interesting to understand if there is a correlation between the shadow size variation and the amount of hair that can be assigned to be outside the shell of FPOs around generic spinning BHs. An investigation on this aspect is underway, and we expect to report on it in the near future.

Acknowledgments

This work was supported by the Center for Research and Development in Mathematics and Applications (CIDMA) through the Portuguese Foundation for Science and Technology (FCT - Fundação para a Ciência e a Tecnologia), references UIDB/04106/2020 and UIDP/04106/2020, by national funds (OE), through FCT, I.P., in the scope of the framework contract foreseen in the numbers

¹⁰We quote this number since it is the thermodynamic limit of energy extraction from superradiance.

4, 5 and 6 of the article 23, of the Decree-Law 57/2016, of August 29, changed by Law 57/2017, of July 19 and by the projects PTDC/FIS-OUT/28407/2017, CERN/FIS-PAR/0027/2019, PTDC/FIS-AST/3041/2020 and CERN/FIS-PAR/0024/2021. This work has further been supported by the European Union’s Horizon 2020 research and innovation (RISE) programme H2020- MSCA-RISE-2017 Grant No. FunFiCO-777740 and by FCT through Project No. UIDB/00099/2020. PC is supported by the Individual CEEC program 2020 funded by the FCT. IS is supported by the FCT grant SFRH/BD/150788/2020 under the IDPASC Doctoral Program. Computations have been performed at the Argus and Blafis cluster at the U. Aveiro.

References

- [1] Carlos A. R. Herdeiro. Black holes: on the universality of the Kerr hypothesis. 4 2022.
- [2] Albert Einstein. Explanation of the Perihelion Motion of Mercury from the General Theory of Relativity. *Sitzungsber. Preuss. Akad. Wiss. Berlin (Math. Phys.)*, 1915:831–839, 1915.
- [3] F. W. Dyson, A. S. Eddington, and C. Davidson. A Determination of the Deflection of Light by the Sun’s Gravitational Field, from Observations Made at the Total Eclipse of May 29, 1919. *Phil. Trans. Roy. Soc. Lond. A*, 220:291–333, 1920.
- [4] Albert Einstein. Lens-Like Action of a Star by the Deviation of Light in the Gravitational Field. *Science*, 84:506–507, 1936.
- [5] Roy P. Kerr. Gravitational field of a spinning mass as an example of algebraically special metrics. *Phys. Rev. Lett.*, 11:237–238, 1963.
- [6] J. M. Bardeen. Timelike and null geodesics in the Kerr metric. In *Les Houches Summer School of Theoretical Physics: Black Holes*, 1973.
- [7] James M. Bardeen, William H. Press, and Saul A Teukolsky. Rotating black holes: Locally nonrotating frames, energy extraction, and scalar synchrotron radiation. *Astrophys. J.*, 178:347, 1972.
- [8] Edward Teo. Spherical photon orbits around a kerr black hole. *General Relativity and Gravitation*, 35(11):1909–1926, November 2003.
- [9] Pedro V. P. Cunha, Carlos A. R. Herdeiro, and Eugen Radu. Fundamental photon orbits: Black hole shadows and spacetime instabilities. *Physical Review D*, 96(2), July 2017.
- [10] J. P. Luminet. Image of a spherical black hole with thin accretion disk. *Astron. Astrophys.*, 75:228–235, 1979.
- [11] Heino Falcke, Fulvio Melia, and Eric Agol. Viewing the shadow of the black hole at the galactic center. *Astrophys. J. Lett.*, 528:L13, 2000.
- [12] Kazunori Akiyama et al. First M87 Event Horizon Telescope Results. I. The Shadow of the Supermassive Black Hole. *Astrophys. J. Lett.*, 875:L1, 2019.

- [13] Kazunori Akiyama et al. First M87 Event Horizon Telescope Results. II. Array and Instrumentation. *Astrophys. J. Lett.*, 875(1):L2, 2019.
- [14] Kazunori Akiyama et al. First M87 Event Horizon Telescope Results. VI. The Shadow and Mass of the Central Black Hole. *Astrophys. J. Lett.*, 875(1):L6, 2019.
- [15] Kazunori Akiyama et al. First Sagittarius A* Event Horizon Telescope Results. I. The Shadow of the Supermassive Black Hole in the Center of the Milky Way. *Astrophys. J. Lett.*, 930(2):L12, 2022.
- [16] Kazunori Akiyama et al. First Sagittarius A* Event Horizon Telescope Results. II. EHT and Multiwavelength Observations, Data Processing, and Calibration. *Astrophys. J. Lett.*, 930(2):L13, 2022.
- [17] Kazunori Akiyama et al. First Sagittarius A* Event Horizon Telescope Results. III. Imaging of the Galactic Center Supermassive Black Hole. *Astrophys. J. Lett.*, 930(2):L14, 2022.
- [18] Kazunori Akiyama et al. First Sagittarius A* Event Horizon Telescope Results. VI. Testing the Black Hole Metric. *Astrophys. J. Lett.*, 930(2):L17, 2022.
- [19] Carlos Herdeiro, Eugen Radu, and Helgi Rúnarsson. Kerr black holes with proca hair. *Classical and Quantum Gravity*, 33(15):154001, June 2016.
- [20] Nuno M. Santos, Carolina L. Benone, Luís C.B. Crispino, Carlos A.R. Herdeiro, and Eugen Radu. Black holes with synchronised proca hair: linear clouds and fundamental non-linear solutions. *Journal of High Energy Physics*, 2020(7), July 2020.
- [21] J. D. Bekenstein. Transcendence of the law of baryon-number conservation in black hole physics. *Phys. Rev. Lett.*, 28:452–455, 1972.
- [22] Richard Brito, Vitor Cardoso, and Paolo Pani. Superradiance: New Frontiers in Black Hole Physics. *Lect. Notes Phys.*, 906:pp.1–237, 2015.
- [23] William E. East and Frans Pretorius. Superradiant Instability and Backreaction of Massive Vector Fields around Kerr Black Holes. *Phys. Rev. Lett.*, 119(4):041101, 2017.
- [24] Carlos A.R. Herdeiro and Eugen Radu. Dynamical formation of kerr black holes with synchronized hair: An analytic model. *Physical Review Letters*, 119(26), Dec 2017.
- [25] Sam Dolan. Spinning Black Holes May Grow Hair. *APS Physics*, 10:83, 2017.
- [26] Richard Brito, Vitor Cardoso, Carlos A.R. Herdeiro, and Eugen Radu. Proca stars: Gravitating bose–einstein condensates of massive spin 1 particles. *Physics Letters B*, 752:291–295, January 2016.
- [27] N. Sanchis-Gual, F. Di Giovanni, M. Zilhão, C. Herdeiro, P. Cerdá-Durán, J. A. Font, and E. Radu. Nonlinear Dynamics of Spinning Bosonic Stars: Formation and Stability. *Phys. Rev. Lett.*, 123(22):221101, 2019.

- [28] Steven L. Liebling and Carlos Palenzuela. Dynamical Boson Stars. *Living Rev. Rel.*, 15:6, 2012.
- [29] Juan Calderón Bustillo, Nicolas Sanchis-Gual, Alejandro Torres-Forné, José A. Font, Avi Vajpeyi, Rory Smith, Carlos Herdeiro, Eugen Radu, and Samson H.W. Leong. Gw190521 as a merger of proca stars: A potential new vector boson of $8.7 \times 10^{-13} \text{ev}$. *Physical Review Letters*, 126(8), Feb 2021.
- [30] Juan Calderon Bustillo, Nicolas Sanchis-Gual, Samson H. W. Leong, Koustav Chandra, Alejandro Torres-Forne, Jose A. Font, Carlos Herdeiro, Eugen Radu, Isaac C. F. Wong, and T. G. F. Li. Searching for vector boson-star mergers within LIGO-Virgo intermediate-mass black-hole merger candidates. 6 2022.
- [31] Carlos A. R. Herdeiro, Alexandre M. Pombo, Eugen Radu, Pedro V. P. Cunha, and Nicolas Sanchis-Gual. The imitation game: Proca stars that can mimic the Schwarzschild shadow. *JCAP*, 04:051, 2021.
- [32] Pedro V.P. Cunha, José A. Font, Carlos Herdeiro, Eugen Radu, Nicolas Sanchis-Gual, and Miguel Zilhão. Lensing and dynamics of ultracompact bosonic stars. *Physical Review D*, 96(10), November 2017.
- [33] Pedro V.P. Cunha, Carlos A.R. Herdeiro, Eugen Radu, and Helgi F. Rúnarsson. Shadows of kerr black holes with scalar hair. *Physical Review Letters*, 115(21), Nov 2015.
- [34] Pedro V. P. Cunha, Carlos A. R. Herdeiro, Eugen Radu, and Helgi F. Rúnarsson. Shadows of kerr black holes with and without scalar hair. *International Journal of Modern Physics D*, 25(09):1641021, August 2016.
- [35] P.V.P. Cunha, J. Grover, C. Herdeiro, E. Radu, H. Rúnarsson, and A. Wittig. Chaotic lensing around boson stars and kerr black holes with scalar hair. *Physical Review D*, 94(10), Nov 2016.
- [36] Pedro Cunha, Carlos Herdeiro, and Eugen Radu. Eht constraint on the ultralight scalar hair of the m87 supermassive black hole. *Universe*, 5(12):220, Nov 2019.
- [37] Asimina Arvanitaki, Savas Dimopoulos, Sergei Dubovsky, Nemanja Kaloper, and John March-Russell. String Axiverse. *Phys. Rev. D*, 81:123530, 2010.
- [38] Felipe F. Freitas, Carlos A. R. Herdeiro, António P. Morais, António Onofre, Roman Pasechnik, Eugen Radu, Nicolas Sanchis-Gual, and Rui Santos. Ultralight bosons for strong gravity applications from simple Standard Model extensions. *JCAP*, 12(12):047, 2021.
- [39] Andy Bohn, William Throwe, François Hébert, Katherine Henriksson, Darius Bunandar, Mark A Scheel, and Nicholas W Taylor. What does a binary black hole merger look like? *Classical and Quantum Gravity*, 32(6):065002, February 2015.
- [40] Mingzhi Wang, Songbai Chen, and Jiliang Jing. Shadows of Bonnor black dihole by chaotic lensing. *Phys. Rev. D*, 97(6):064029, 2018.
- [41] Mingzhi Wang, Songbai Chen, and Jiliang Jing. Chaotic shadow of a non-Kerr rotating compact object with quadrupole mass moment. *Phys. Rev. D*, 98(10):104040, 2018.

- [42] Pedro V. P. Cunha, Carlos A. R. Herdeiro, and Maria J. Rodriguez. Does the black hole shadow probe the event horizon geometry? *Phys. Rev. D*, 97(8):084020, 2018.
- [43] Jai Grover, Jutta Kunz, Petya Nedkova, Alexander Wittig, and Stoytcho Yazadjiev. Multiple shadows from distorted static black holes. *Phys. Rev. D*, 97(8):084024, 2018.
- [44] Pedro V. P. Cunha, Carlos A. R. Herdeiro, and Maria J. Rodriguez. Shadows of Exact Binary Black Holes. *Phys. Rev. D*, 98(4):044053, 2018.
- [45] Pedro V. P. Cunha, Carlos A. R. Herdeiro, and Eugen Radu. Isolated black holes without \mathbb{Z}_2 isometry. *Phys. Rev. D*, 98(10):104060, 2018.
- [46] Mingzhi Wang, Songbai Chen, Jieci Wang, and Jiliang Jing. Shadow of a Schwarzschild black hole surrounded by a Bach–Weyl ring. *Eur. Phys. J. C*, 80(2):110, 2020.
- [47] Songbai Chen, Mingzhi Wang, and Jiliang Jing. Polarization effects in Kerr black hole shadow due to the coupling between photon and bumblebee field. *JHEP*, 07:054, 2020.
- [48] Haroldo C. D. Lima, Junior., Luís C. B. Crispino, Pedro V. P. Cunha, and Carlos A. R. Herdeiro. Can different black holes cast the same shadow? *Phys. Rev. D*, 103(8):084040, 2021.
- [49] Fabio Bacchini, Daniel R. Mayerson, Bart Ripperda, Jordy Davelaar, Héctor Olivares, Thomas Hertog, and Bert Vercoocke. Fuzzball Shadows: Emergent Horizons from Microstructure. *Phys. Rev. Lett.*, 127(17):171601, 2021.
- [50] Haroldo C. D. Lima Junior, Pedro V. P. Cunha, Carlos A. R. Herdeiro, and Luís C. B. Crispino. Shadows and lensing of black holes immersed in strong magnetic fields. *Phys. Rev. D*, 104(4):044018, 2021.
- [51] Mingzhi Wang, Songbai Chen, and Jiliang Jing. Kerr black hole shadows in Melvin magnetic field with stable photon orbits. *Phys. Rev. D*, 104(8):084021, 2021.
- [52] Zhen Zhong, Zezhou Hu, Haopeng Yan, Minyong Guo, and Bin Chen. QED effects on Kerr black hole shadows immersed in uniform magnetic fields. *Phys. Rev. D*, 104(10):104028, 2021.
- [53] Mingzhi Wang, Guanghai Guo, Songbai Chen, and Jiliang Jing. The surface geometry and shadow of a Schwarzschild black hole with halo. 12 2021.
- [54] Mingzhi Wang, Songbai Chen, and Jiliang Jing. Chaotic Shadows of Black Holes: A Short Review. 5 2022.
- [55] Vitor Cardoso, Luís C.B. Crispino, Caio F.B. Macedo, Hirotada Okawa, and Paolo Pani. Light rings as observational evidence for event horizons: Long-lived modes, ergoregions and nonlinear instabilities of ultracompact objects. *Physical Review D*, 90(4), Aug 2014.
- [56] Pedro V. P. Cunha, Carlos Herdeiro, Eugen Radu, and Nicolas Sanchis-Gual. The fate of the light-ring instability. 7 2022.
- [57] Rajes Ghosh and Sudipta Sarkar. Light rings of stationary spacetimes, 2021.

- [58] Elisa Maggio, Vitor Cardoso, Sam R. Dolan, and Paolo Pani. Ergoregion instability of exotic compact objects: Electromagnetic and gravitational perturbations and the role of absorption. *Physical Review D*, 99(6), Mar 2019.
- [59] Joe Keir. Slowly decaying waves on spherically symmetric spacetimes and ultracompact neutron stars. *Class. Quant. Grav.*, 33(13):135009, 2016.
- [60] Pedro V.P. Cunha, Emanuele Berti, and Carlos A.R. Herdeiro. Light-ring stability for ultracompact objects. *Physical Review Letters*, 119(25), Dec 2017.
- [61] Wei-Liang Qian, Songbai Chen, Cheng-Gang Shao, Bin Wang, and Rui-Hong Yue. Cuspy and fractured black hole shadows in a toy model with axisymmetry. *Eur. Phys. J. C*, 82(1):91, 2022.
- [62] Pedro V. P. Cunha and Carlos A. R. Herdeiro. Shadows and strong gravitational lensing: a brief review. *General Relativity and Gravitation*, 50(4), Mar 2018.
- [63] Pedro V.P. Cunha and Carlos A.R. Herdeiro. Stationary black holes and light rings. *Physical Review Letters*, 124(18), May 2020.
- [64] Carlos A.R. Herdeiro, Eugen Radu, and Nuno M. Santos. A bound on energy extraction (and hairiness) from superradiance. *Physics Letters B*, 824:136835, jan 2022.
- [65] Juan Carlos Degollado, Carlos A.R. Herdeiro, and Eugen Radu. Effective stability against superradiance of kerr black holes with synchronised hair. *Physics Letters B*, 781:651–655, Jun 2018.
- [66] Nicolas Sanchis-Gual, Miguel Zilhão, Carlos Herdeiro, Fabrizio Di Giovanni, José A. Font, and Eugen Radu. Synchronized gravitational atoms from mergers of bosonic stars. *Phys. Rev. D*, 102(10):101504, 2020.
- [67] Kazunori Akiyama et al. First M87 Event Horizon Telescope Results. I. The Shadow of the Supermassive Black Hole. *Astrophys. J. Lett.*, 875:L1, 2019.
- [68] R. Craig Walker, Phillip E. Hardee, Frederick B. Davies, Chun Ly, and William Junor. The Structure and Dynamics of the Subparsec Jet in M87 Based on 50 VLBA Observations over 17 Years at 43 GHz. *Astrophys. J.*, 855(2):128, 2018.
- [69] Nicolas Sanchis-Gual, Miguel Zilhã o, Carlos Herdeiro, Fabrizio Di Giovanni, José A. Font, and Eugen Radu. Synchronized gravitational atoms from mergers of bosonic stars. *Physical Review D*, 102(10), nov 2020.
- [70] S.W. Hawking. Gravitational Radiation from Colliding Black Holes. *PRL*, 26(21):1344–1346, May 1971.
- [71] Karl Gebhardt, Joshua Adams, Douglas Richstone, Tod R. Lauer, S. M. Faber, Kayhan Gültekin, Jeremy Murphy, and Scott Tremaine. The Black Hole Mass in M87 from Gemini/NIFS Adaptive Optics Observations. *ApJ*, 729(2):119, March 2011.

- [72] Jonelle L. Walsh, Aaron J. Barth, Luis C. Ho, and Marc Sarzi. The M87 Black Hole Mass from Gas-dynamical Models of Space Telescope Imaging Spectrograph Observations. *ApJ*, 770(2):86, June 2013.
- [73] Gravity Collaboration, R. Abuter, N. Aimar, A. Amorim, J. Ball, M. Bauböck, J. P. Berger, H. Bonnet, G. Bourdarot, W. Brandner, V. Cardoso, Y. Clénet, Y. Dallilar, R. Davies, P. T. de Zeeuw, J. Dexter, A. Drescher, F. Eisenhauer, N. M. Förster Schreiber, A. Foschi, P. Garcia, F. Gao, E. Gendron, R. Genzel, S. Gillessen, M. Habibi, X. Haubois, G. Heißel, T. Henning, S. Hippler, M. Horrobin, L. Jochum, L. Jocou, A. Kaufer, P. Kervella, S. Lacour, V. Lapeyrère, J. B. Le Bouquin, P. Léna, D. Lutz, T. Ott, T. Paumard, K. Perraut, G. Perrin, O. Pfuhl, S. Rabien, J. Shangguan, T. Shimizu, S. Scheithauer, J. Stadler, A. W. Stephens, O. Straub, C. Straubmeier, E. Sturm, L. J. Tacconi, K. R. W. Tristram, F. Vincent, S. von Fellenberg, F. Widmann, E. Wieprecht, E. Wiezorrek, J. Woillez, S. Yazici, and A. Young. Mass distribution in the Galactic Center based on interferometric astrometry of multiple stellar orbits. *Aap*, 657:L12, January 2022.
- [74] T. Do, A. M. Ghez, M. R. Morris, S. Yelda, L. Meyer, J. R. Lu, S. D. Hornstein, and K. Matthews. A Near-Infrared Variability Study of the Galactic Black Hole: A Red Noise Source with NO Detected Periodicity. *ApJ*, 691(2):1021–1034, February 2009.
- [75] V. I. Dokuchaev and N. O. Nazarova. Visible shapes of black holes M87* and SgrA*. *Universe*, 6(9):154, 2020.
- [76] Sebastian H. Völkel, Enrico Barausse, Nicola Franchini, and Avery E. Broderick. EHT tests of the strong-field regime of general relativity. *Class. Quant. Grav.*, 38(21):21LT01, 2021.
- [77] Mohsen Khodadi, Alireza Allahyari, Sunny Vagnozzi, and David F. Mota. Black holes with scalar hair in light of the Event Horizon Telescope. *JCAP*, 09:026, 2020.
- [78] Kostas Glampedakis and George Pappas. Can supermassive black hole shadows test the Kerr metric? *Phys. Rev. D*, 104(8):L081503, 2021.
- [79] Shafqat Ul Islam and Sushant G. Ghosh. Strong field gravitational lensing by hairy Kerr black holes. *Phys. Rev. D*, 103(12):124052, 2021.
- [80] Shao-Wen Wei and Yuan-Chuan Zou. Constraining rotating black hole via curvature radius with observations of M87*. 8 2021.
- [81] Misba Afrin, Rahul Kumar, and Sushant G. Ghosh. Parameter estimation of hairy Kerr black holes from its shadow and constraints from M87*. *Mon. Not. Roy. Astron. Soc.*, 504:5927–5940, 2021.
- [82] Misba Afrin and Sushant G. Ghosh. Testing Horndeski Gravity from EHT Observational Results for Rotating Black Holes. *Astrophys. J.*, 932(1):51, 2022.
- [83] Guillermo Lara, Sebastian H. Völkel, and Enrico Barausse. Separating astrophysics and geometry in black hole images. *Phys. Rev. D*, 104(12):124041, 2021.

- [84] Yuan Meng, Xiao-Mei Kuang, and Zi-Yu Tang. Photon regions, shadow observables and constraints from M87* of a charged rotating black hole. 4 2022.
- [85] Xiao-Mei Kuang and Ali Övgün. Strong gravitational lensing and shadow constraint from M87* of slowly rotating Kerr-like black hole. 5 2022.
- [86] Sushant G. Ghosh and Misba Afrin. Constraining Kerr-like black holes with Event Horizon Telescope results of Sgr A*. 6 2022.
- [87] Akash Kumar Saha, Priyank Parashari, Tarak Nath Maity, Abhishek Dubey, Subhadip Bouri, and Ranjan Laha. Bounds on ultralight bosons from the Event Horizon Telescope observation of Sgr A*. 8 2022.
- [88] Ahmadjon Abdujabbarov, Muhammed Amir, Bobomurat Ahmedov, and Sushant G. Ghosh. Shadow of rotating regular black holes. *Phys. Rev. D*, 93(10):104004, 2016.
- [89] F. H. Vincent, E. Gourgoulhon, C. Herdeiro, and E. Radu. Astrophysical imaging of Kerr black holes with scalar hair. *Phys. Rev. D*, 94(8):084045, 2016.
- [90] Pedro V.P. Cunha, Carlos A.R. Herdeiro, Burkhard Kleihaus, Jutta Kunz, and Eugen Radu. Shadows of einstein–dilatons–gauss–bonnet black holes. *Physics Letters B*, 768:373–379, May 2017.
- [91] Dimitry Ayzenberg and Nicolas Yunes. Black Hole Shadow as a Test of General Relativity: Quadratic Gravity. *Class. Quant. Grav.*, 35(23):235002, 2018.
- [92] Xian Hou, Zhaoyi Xu, and Jiancheng Wang. Rotating Black Hole Shadow in Perfect Fluid Dark Matter. *JCAP*, 12:040, 2018.
- [93] Hui-Min Wang, Yu-Meng Xu, and Shao-Wen Wei. Shadows of Kerr-like black holes in a modified gravity theory. *JCAP*, 03:046, 2019.
- [94] Rajibul Shaikh. Black hole shadow in a general rotating spacetime obtained through Newman-Janis algorithm. *Phys. Rev. D*, 100(2):024028, 2019.
- [95] Ernesto Contreras, J. M. Ramirez-Velasquez, Ángel Rincón, Grigoris Panotopoulos, and Pedro Bargueño. Black hole shadow of a rotating polytropic black hole by the Newman–Janis algorithm without complexification. *Eur. Phys. J. C*, 79(9):802, 2019.
- [96] Rittick Roy and Urjit A. Yajnik. Evolution of black hole shadow in the presence of ultralight bosons. *Phys. Lett. B*, 803:135284, 2020.
- [97] Ernesto Contreras, Ángel Rincón, Grigoris Panotopoulos, Pedro Bargueño, and Benjamin Koch. Black hole shadow of a rotating scale–dependent black hole. *Phys. Rev. D*, 101(6):064053, 2020.
- [98] Zhe Chang and Qing-Hua Zhu. Revisiting a rotating black hole shadow with astrometric observables. *Phys. Rev. D*, 101(8):084029, 2020.

- [99] Shao-Wen Wei and Yu-Xiao Liu. Testing the nature of Gauss-Bonnet gravity by four-dimensional rotating black hole shadow. *Eur. Phys. J. Plus*, 136(4):436, 2021.
- [100] Sérgio Vinicius M. C. B. Xavier, Pedro V. P. Cunha, Luís C. B. Crispino, and Carlos A. R. Herdeiro. Shadows of charged rotating black holes: Kerr–Newman versus Kerr–Sen. *Int. J. Mod. Phys. D*, 29(11):2041005, 2020.
- [101] Che-Yu Chen. Rotating black holes without \mathbb{Z}_2 symmetry and their shadow images. *JCAP*, 05:040, 2020.
- [102] Gastón Creci, Stefan Vandoren, and Helvi Witek. Evolution of black hole shadows from super-radiance. *Phys. Rev. D*, 101(12):124051, 2020.
- [103] Bum-Hoon Lee, Wonwoo Lee, and Yun Soo Myung. Shadow cast by a rotating black hole with anisotropic matter. *Phys. Rev. D*, 103(6):064026, 2021.
- [104] Javier Badía and Ernesto F. Eiroa. Shadow of axisymmetric, stationary, and asymptotically flat black holes in the presence of plasma. *Phys. Rev. D*, 104(8):084055, 2021.
- [105] Mingzhi Wang, Songbai Chen, and Jiliang Jing. Shadow casted by a Konoplya-Zhidenko rotating non-Kerr black hole. *JCAP*, 10:051, 2017.
- [106] Igor Bogush, Dmitri Gal'tsov, Galin Gyulchev, Kirill Kobialko, Petya Nedkova, and Tsvetan Vetsov. Photon surfaces, shadows, and accretion disks in gravity with minimally coupled scalar field. *Phys. Rev. D*, 106(2):024034, 2022.
- [107] Volker Perlick and Oleg Yu. Tsupko. Calculating black hole shadows: Review of analytical studies. *Phys. Rept.*, 947:1–39, 2022.

A Physical quantities of selected solutions

Label	ω	$M\mu$	$J\mu^2$	$M_{BH}\mu$	$J_{BH}\mu^2$	M_{BH}/M	J_{BH}/J	J/M^2	J_{BH}/M_{BH}^2
3.4	0.95	0.317	0.120	0.242	0.048	0.763	0.402	1.194	0.825
3.3	0.95	0.422	0.314	0.114	0.007	0.269	0.023	1.764	0.555
3.2	0.95	0.482	0.435	0.051	0.001	0.107	0.002	1.874	0.279
3.1	0.95	0.528	0.532	0.005	0.000	0.009	0.000	1.905	0.033
6.4	0.8	0.744	0.620	0.142	0.036	0.191	0.058	1.118	1.777
6.3	0.8	0.601	0.383	0.351	0.169	0.585	0.442	1.061	1.371
6.2	0.8	0.865	0.842	0.054	0.003	0.062	0.003	1.125	1.009
6.1	0.8	0.938	0.992	0.005	0.000	0.005	0.000	1.126	0.116
7.3	0.75	0.820	0.719	0.118	0.035	0.144	0.048	1.069	2.497
7.2	0.75	0.947	0.958	0.043	0.003	0.045	0.003	1.068	1.409
7.1	0.75	1.005	1.076	0.005	0.000	0.005	0.000	1.066	0.198
8.3	0.7	0.896	0.833	0.084	0.026	0.093	0.031	1.037	3.653
8.2	0.7	0.937	0.908	0.060	0.012	0.064	0.013	1.035	3.265
8.1	0.7	1.052	1.140	0.005	0.000	0.005	0.000	1.030	0.371
9.3	0.65	0.997	1.007	0.037	0.007	0.037	0.007	1.014	4.895
9.2	0.65	1.041	1.096	0.020	0.001	0.020	0.001	1.011	3.024
9.1	0.65	1.083	1.184	0.005	0.000	0.004	0.000	1.009	0.800
10.3	0.6	1.000	1.005	0.036	0.013	0.036	0.013	1.005	10.251
10.2	0.6	1.057	1.119	0.016	0.002	0.015	0.001	1.002	6.674
10.1	0.6	1.099	1.206	0.005	0.000	0.004	0.000	0.999	2.198

Table 4: Physical quantities of the KBHsPH solutions highlighted in Figure 1.

Label	ω	$M\mu$	$J\mu^2$
1.0	0.99	0.246	0.247
2.0	0.97	0.420	0.424
3.0	0.95	0.533	0.542
4.0	0.9	0.725	0.749
5.0	0.85	0.853	0.896
6.0	0.8	0.946	1.007
7.0	0.75	1.014	1.095
8.0	0.7	1.063	1.162
9.0	0.65	1.096	1.212
10.0	0.6	1.117	1.245
11.0	0.55	1.124	1.256
12.0	0.5	1.112	1.234
13.0	0.47	1.091	1.189

Table 5: Physical quantities of the Proca star solutions highlighted in Figure 1.